Dynamics of a stratified shear layer above a region of uniform stratification

HIEU T. PHAM, SUTANU SARKAR†
AND KYLE A. BRUCKER

Mechanical and Aerospace Engineering, University of California, San Diego, La Jolla,
CA 92093, USA

Direct numerical simulations (DNS) are performed to investigate the behaviour of a weakly stratified shear layer in the presence of a strongly stratified region beneath it. Both, coherent Kelvin–Helmholtz (KH) rollers and small-scale turbulence, are observed during the evolution of the shear layer. The deep stratification measured by the Richardson number J_d is varied to study its effect on the dynamics. In all cases, a pycnocline is found to develop at the edges of the shear layer. The region of maximum shear shifts downward with increasing time. Internal waves are excited, initially by KH rollers, and later by small-scale turbulence. The wave field generated by the KH rollers is narrowband and of stronger amplitude than the broadband wave field generated by turbulence. Linear theory based on Doppler-shifted frequency of the KH mode is able to predict the angle of the internal wave phase lines during the direct generation of internal waves by KH rollers. Waves generated by turbulence are relatively weaker with a broader range of excitation angles which, in the deep region, tend towards a narrower band. The linear theory that works for the internal waves excited by KH rollers does not work for the turbulence generated waves. The momentum transported by the internal waves into the interior can be large, about 10 % of the initial momentum in the shear layer, when $J_d \simeq 0.25$. Integration of the turbulent kinetic energy budget in time and over the shear layer thickness shows that the energy flux can be up to 17 % of the turbulent production, 33 % of the turbulent dissipation rate and 75 % of the buoyancy flux. These numbers quantify the dynamical importance of internal waves. In contrast to linear theory where the effect of deep stratification on the shear layer instabilities has been found to be weak, the present nonlinear simulations show that the evolution of the shear layer is significantly altered because of the significant momentum and energy carried away by the internal waves.

1. Introduction

Stratified shear flow away from boundaries has been the subject of many studies, employing both experimental and numerical techniques. Nevertheless, there are only a handful that study the dynamics of a stratified shear layer in the presence of an external stratification where internal waves may be supported. Such a scenario can occur in the natural environment when the stratification extends continuously beyond the shear layer, and will be the focus of the current study.

† Email address for correspondence: ssarkar@ucsd.edu

Laboratory experiments, for example, Thorpe (1973) and Koop & Browand (1979), were the earliest systematic studies of instability and turbulence in a stratified shear layer. In those studies, the shear zone was between two layers of constant density and the mean shear was inflectional. Rohr *et al.* (1988) performed experiments of homogeneous shear flow turbulence (constant value of shear S and stratification N) using a salt-stratified water channel. Piccirillo & VanAtta (1997) studied the same problem using a thermally stratified wind tunnel, and numerical simulations were performed by Gerz, Schumann & Elghobashi (1989), Holt, Koseff & Ferziger (1992), Kaltenbach, Gerz & Schumann (1994), Jacobitz, Sarkar & VanAtta (1997), Jacobitz & Sarkar (1999*b*) and Diamessis & Nomura (2004). Numerical simulations of the stratified shear layer (or mixing layer) between two streams with a velocity difference have been performed using small-amplitude initial perturbations to understand the role of stratification by Staquet & Riley (1989), Caulfield & Peltier (1994, 2000), Smyth & Moum (2000*a*,*b*), Staquet (2000) and Smyth, Moum & Caldwell (2001) and, more recently, by Brucker & Sarkar (2007) who examined buoyancy effects when the initial perturbations are turbulent. A stratified shear layer may have horizontal shear in contrast to the vertical shear common to all the aforementioned studies. The constant-shear example of horizontal shear was studied numerically by Jacobitz & Sarkar (1999*a*) while Basak & Sarkar (2006) and Deloncle, Chomaz & Billant (2007) have studied the case of inflectional horizontal shear.

Internal waves generated by unstable velocity shears have been observed in previous atmospheric and oceanic studies. Wind shear is believed to be one of the principal sources of internal wave excitation in the lower atmosphere (Einaudi, Lalas & Perona 1978, 1979). Internal waves observed in the mesosphere (Holton *et al.* 1995) and in the upper stratosphere (Rosenlof 1996) are excited by non-orographic sources, for example the Kelvin–Helmholtz (KH) instability, since orographic waves cannot reach these altitudes. Below the surface of the equatorial oceans, alternating eastward and westward currents (Luyten & Swallow 1976; Eriksen 1982; Firing 1987) are observed. Eriksen (1982) has observed large-scale structures of the countercurrents persisting for a long period of time. Moum *et al.* (1992) and Sun, Smyth & Moum (1998) suggest that internal waves associated with the equatorial undercurrent can be the main source of mixing in the thermocline. Since internal waves can transport and redistribute momentum and energy (Eliassen & Palm 1960; Andrews & McIntyre 1978; Fritts 1982), it becomes necessary to examine the transport of the internal waves excited by unstable shears.

A stratified shear layer with weak stratification of value J_0, non-dimensionalized with the maximum shear, that overlies an adjacent region with stronger stratification J_d has been investigated using linear theory and two-dimensional nonlinear simulations by Sutherland (1996). Internal waves are found to radiate downward from the shear layer and propagate in the deep far field. It is found that internal waves are generated by the most unstable linear mode and, from the two-dimensional simulations that track the evolution of a KH billow, it is concluded that strong internal waves are excited when $J_0 < 0.25$ and $J_d > 0.25$. Sutherland (2006) examined the evolution of a shear layer (also a jet) with asymmetric stratification, using linear theory and two-dimensional simulations. The distance δ between the shear layer and the top of the stratified region was varied along with the values of J_d. For small δ, the shear layer instability mode was found to directly couple to the internal wave mode and its subsequent nonlinear evolution was significantly modified. Simulations of a jet with asymmetric stratification have been performed in two dimensions by Skyllingstad & Denbo (1994) and Smyth & Moum (2002) to model aspects of

the equatorial undercurrent and using three-dimensional DNS by Tse *et al.* (2003) as a model for the jet at the atmospheric tropopause. Skyllingstad & Denbo (1994) in a problem forced with wind stress and buoyancy flux identify local instabilities as well as internal wave packets. Smyth & Moum (2002) consider a Bickley jet with low stratification J_U in the upper half and high stratification J_L in the lower half. Their simulations of cases with $J_U = 0.0$ and 0.05, and $J_L = 0.25$ show energetic internal waves directed downward away from the jet. Tse *et al.* (2003) perform three-dimensional simulations where the velocity and temperature profiles of the base flow, constructed to model a jet in the atmospheric tropopause, are forced. A quasi-equilibrium jet results with strong shear-forced turbulence in the core of the jet where the gradient Richardson number $Ri_g \ll 0.25$. The edges of the jet, with moderate-to-large values of Ri_g, have patchy turbulence, attributed to nonlinear wave activity. Propagation of internal waves in the jet far field is not significant. It is found that the change of the fluctuations from mechanical turbulence in the core to stratified turbulence at the edges can be effectively characterized through length scales and through budget equations for the velocity and temperature variances.

The effect of internal waves on the deepening of a mixed layer in a stratified fluid was studied by Linden (1975). An oscillating grid was used to generate a turbulent mixed layer on top of a layer with a constant density gradient. As the mixed layer deepened, the density gradient was observed to increase to a maximum in the thermocline. Internal waves were observed to propagate away from the mixed layer. These waves caused a loss of energy available for mixing. The experiment estimated up to 50 % reduction in the mixing rate due to the presence of internal waves. A similar study carried out by E & Hopfinger (1986) compared the deepening rate between a two-layer and a constant density gradient systems. Internal waves radiating energy away from the interface only occurred in the latter case. The energy radiation was found not to significantly affect the mass entrainment rate, defined by $E = (1/u)\mathrm{d}D(t)/\mathrm{d}t$ with D the mixed layer depth and u the r.m.s. velocity fluctuation. The coefficients K and n in the entrainment rate relation $E = K\,Ri^{-n}$ were found to be the same in both cases, independent of the presence of internal waves.

Internal wave propagation was also observed in the experiments of Strang & Fernando (2001) designed to study turbulent entrainment and mixing at a sheared density interface. A shear layer separated a light upper well-mixed turbulent layer from a lower quiescent layer which was either constant density or linearly stratified. Internal waves only appeared in the latter case. When the lower layer was linearly stratified, 'interfacial swelling' in the shear layer was observed and argued to be responsible for internal wave excitation. The buoyancy flux and the entrainment rate were higher when internal waves did not propagate into the lower layer. The mass entrainment rate was reduced by as much as 50 % in the presence of internal waves. The ratio of the wave energy flux to the rate of change of potential energy due to mixed-layer deepening was found to be approximately 48 %.

Sutherland & Linden (1998) quantified the effects of internal waves in an experimental investigation of stratified fluid with shear that flows over a thin barrier. In the experiment, the upper region was lightly stratified while the lower region had a higher density gradient. Vortices, shed in the wake of the thin barrier, disturbed the base of the sheared mixing region and internal waves were observed to radiate downward. The propagating waves made angles to the vertical in the range of 45°–60°. The Reynolds stress was measured and it was found that approximately 7 % of the average momentum across the shear depth was lost due to wave transport. A
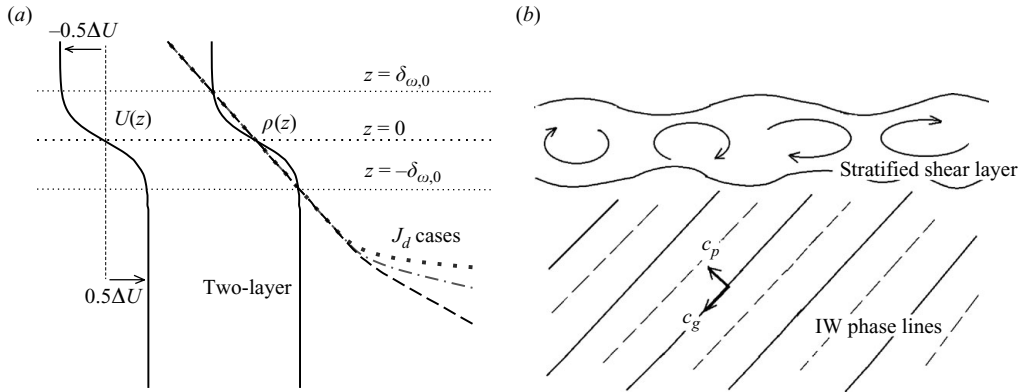
FIGURE 1. (*a*) *Initial* mean profiles. Each case has a temporally evolving shear layer between two streams with velocities $-\Delta U/2$ and $\Delta U/2$, and initial vorticity thickness $\delta_{\omega,0}$. The maximum shear is at $z = 0$. The two-layer density variation corresponds to a tangent-hyperbolic profile with $J(0) = 0.1$. The other density profiles correspond to a moderate linear stratification, $J_s = 0.05$, in the shear layer above a bottom region, $z < -2.5\delta_{\omega,0}$, with uniform deep stratification that takes the values: $J_d = 0.1$, 0.25 and 1.0. The initial value of bulk Richardson number $Ri_{b,0} = 0.1$ is the same for all cases. (*b*) Cartoon of internal wave excitation by shear layer instabilities. The indicated group and phase velocity are relative to the lower free stream.

two-dimensional numerical simulation was also performed. The simulation showed a higher value of the momentum extraction from the mean flow. The authors proposed that internal waves propagating at nearly 45° angle with the vertical were preferred since, through nonlinear interaction, they were capable of modifying the mean flow in a manner which fostered their continual generation.

In the present study, we use direct numerical simulations (DNS) to investigate the problem of an inhomogeneous stratified shear layer located between a weakly stratified upper layer and strongly stratified lower layer (schematic illustration in figure 1). Unlike previous simulations of this shear layer configuration, the present three-dimensional study allows the examination of internal wave dynamics in the presence of realistic turbulent mixing. The flow is seeded with small-amplitude perturbations. The deep stratification is varied to elucidate its effect on the evolution of both the sheared region and the internal wave field. We examine the DNS results to help answer the following questions: How does the thickening of the shear layer depend on deep stratification? Does linear theory provide guidance to characterize the internal waves in these fully nonlinear three-dimensional simulations? What are the relative roles of KH rollers and small-scale three-dimensional turbulence insofar as internal waves? Are the mass flux, momentum flux and energy flux carried away by the internal waves significant?

2. Formulation

Figure 1 is a schematic illustration of the simulated shear layer between two layers of fluid moving in opposite directions with a velocity difference ΔU^* and a vertical density stratification owing to a temperature variation. The flow evolves temporally with statistics that are homogeneous in the streamwise (x) and spanwise (y) directions. The horizontal velocity varies continuously in the vertical cross-stream direction (z)

with a hyperbolic tangent profile,

$$\langle u^* \rangle = -\frac{\Delta U^*}{2} \tanh\left(\frac{2z^*}{\delta_{\omega,0}^*}\right),$$

where the initial vorticity thickness is defined by $\delta_{\omega,0}^* = \Delta U^*/(\mathrm{d}\langle u^* \rangle/\mathrm{d}z^*)_{max}$. Here, the superscript * denotes dimensional quantities. The squared buoyancy frequency is defined by $N^{*2} = -(g^*/\rho_0^*)\mathrm{d}\langle \rho^* \rangle/\mathrm{d}z^*$ and a non-dimensional measure of the stratification is the Richardson number, $J(z) = N^*(z^*)^2\delta_{\omega,0}^{*2}/\Delta U^{*2}$. Two types of density profile are considered. A two-layer density variation, corresponding to the classical Thorpe problem, is defined with a tangent-hyperbolic profile obtained by replacing ΔU^* in the mean velocity profile with the density change $\Delta \rho^*$. The value of $\Delta \rho^*$ is chosen to set $J(z=0) = 0.1$. The second type of density profile corresponds to a weakly stratified shear layer above a region of deep stratification. The fluid above and inside the shear layer region is linearly stratified with Richardson number, $J_s = 0.05$. At depth $z^* = -2.5\delta_{\omega,0}^*$ the stratification changes to the value of the Richardson number specified in the deep region, J_d. Three simulations are performed with deep stratification, $J_d = 0.1$, 0.25 and 1.0. According to linear analysis, the smallest J_d case does not permit propagating internal waves while the other two do. The density profiles are chosen so that the value of the bulk Richardson number Ri_b defined by (2.4) for a shear layer has the same initial value for all four simulations.

The initial vorticity thickness $\delta_{\omega,0}^*$, the density jump $\Delta \rho_0^*$ across twice the initial vorticity thickness and the velocity difference ΔU^* are used for non-dimensionalization. Henceforth, u, x, y, z, p, ρ, t will denote non-dimensional variables and, with the Boussinesq approximation, the governing equations can be written as follows:

$$\frac{\partial u_k}{\partial x_k} = 0, \tag{2.1}$$

$$\frac{\partial u_i}{\partial t} + \frac{\partial (u_k u_i)}{\partial x_k} = -\frac{\partial p}{\partial x_i} + \frac{1}{Re_0}\frac{\partial^2 u_i}{\partial x_k \partial x_k} - Ri_{b,0}\rho'\delta_{i3}, \tag{2.2}$$

$$\frac{\partial \rho}{\partial t} + \frac{\partial (u_k \rho)}{\partial x_k} = \frac{1}{Re_0 Pr}\frac{\partial^2 \rho}{\partial x_k \partial x_k}, \tag{2.3}$$

where

$$Re_0 = \frac{\Delta U^* \delta_{\omega,0}^*}{\nu^*}, \quad Ri_{b,0} = \frac{g^* \Delta \rho_0^* \delta_{\omega,0}^*}{\rho_0^* \Delta U^{*2}} = g\frac{\Delta \rho_0^*}{\rho_0^*}, \quad Pr = \frac{\nu^*}{\kappa^*}. \tag{2.4}$$

Here, ν^* is the kinematic viscosity and κ^* is the molecular diffusivity. The initial bulk Richardson number can be interpreted as a ratio of potential energy to kinetic energy or, alternatively, non-dimensional reduced gravity. Subscript 0 denotes a value at initial time. All simulations are run with $Re_0 = 1280$, $Pr = 1$ and $Ri_{b,0} = 0.1$. Although thermally stratified water has $Pr = 5\text{--}10$ depending on water temperature, we choose $Pr = 1$ to avoid the increase in computational resources, necessary at high Pr. The evolution of the shear layer at different values of J_d is examined. Three simulations are performed with $J_d = 0.1, 0.25$ and 1.0. A two-layer stratified shear layer is also simulated at the same initial Re_0, Pr and $Ri_{b,0}$ for comparison.

The domain size is $51.6 \times 17.2 \times 96.57$ and the numbers of gridpoints in x, y, z directions are $384 \times 128 \times 512$, respectively. The grid is uniform in the streamwise and spanwise directions with a spacing of 0.134. In the vertical direction the grid is uniform in the region $-7.5 \leqslant z \leqslant 2.5$ with a spacing of 0.0756. Outside this region the grid is mildly stretched at ratio of 2 % giving a maximum spacing of 0.475.

A second-order finite difference method on a staggered grid is used for spatial derivatives and a third-order low storage Runge–Kutta method is used for time advancement. The flow is initialized with low amplitude velocity perturbations. These fluctuations have an initial broadband spectrum given by

$$E(k) \propto k^4 \exp\left[-2\left(\frac{k}{k_0}\right)^2\right],$$

where k_0 is set such that the spectrum peaks at 1.7. The initial velocity fluctuations are introduced in the shear layer with the peak values set at 1 % (ΔU). The noise is restricted to the shear region with the shape function $A(z)$, where

$$A(z) = \exp(-z^2).$$

Periodic boundary conditions are used in the streamwise and spanwise directions. Dirichlet boundary conditions are enforced for horizontal velocities and pressure while vertical velocity and density have the following Neumann conditions:

$$u(z_{min}) = \frac{1}{2}, \quad u(z_{max}) = -\frac{1}{2},$$
$$v(z_{min}) = v(z_{max}) = 0,$$
$$p(z_{min}) = p(z_{max}) = 0,$$
$$\frac{\partial w}{\partial z}(z_{min}) = \frac{\partial w}{\partial z}(z_{max}) = 0,$$
$$\frac{\partial \rho}{\partial z}(z_{max}) = -\frac{J_s}{g},$$
$$\frac{\partial \rho}{\partial z}(z_{min}) = -\frac{J_d}{g}.$$

A sponge region is employed at the top ($z > z_{max}^t = 15$) and the bottom ($z < z_{min}^t = -50$) boundaries to control spurious reflections of internal waves propagating out of the domain. The test domain of interest, $z_{min}^t < z < z_{max}^t$, excludes the sponge region. The velocities and density in the sponge region are relaxed by adding to the right-hand side of (2.2) and (2.3) a term of the form

$$-\phi(z)[u_i(x_i, t) - \langle u \rangle_i(z, t = 0)],$$
$$-\phi(z)[\rho(x_i, t) - \langle \rho \rangle(z, t = 0)].$$

The damping function $\phi(z)$ increases quadratically from $\phi = 0$ to 1.0 in a region of thickness 15 utilizing 30 gridpoints at each boundary. Flow instabilities, notably KH rollers, form followed by a transition into small-scale three-dimensional turbulence. Simulations are continued until most of the fluctuation energy inside the shear layer is dissipated, roughly at $t_f = 250$ time units ($\delta_{\omega,0}^*/\Delta U^*$). Details of the numerical methods used in this study can be found in Basak & Sarkar (2006) and Brucker & Sarkar (2007).

3. Evolution of the shear layer

The KH instability mode is initially amplified, KH rollers develop, secondary instabilities follow and, finally, there is breakdown to three-dimensional turbulence (Thorpe 1973; Koop & Browand 1979; Staquet & Riley 1989; Caulfield & Peltier 2000; Smyth & Moum 2000b). In the following text, we show the strong influence
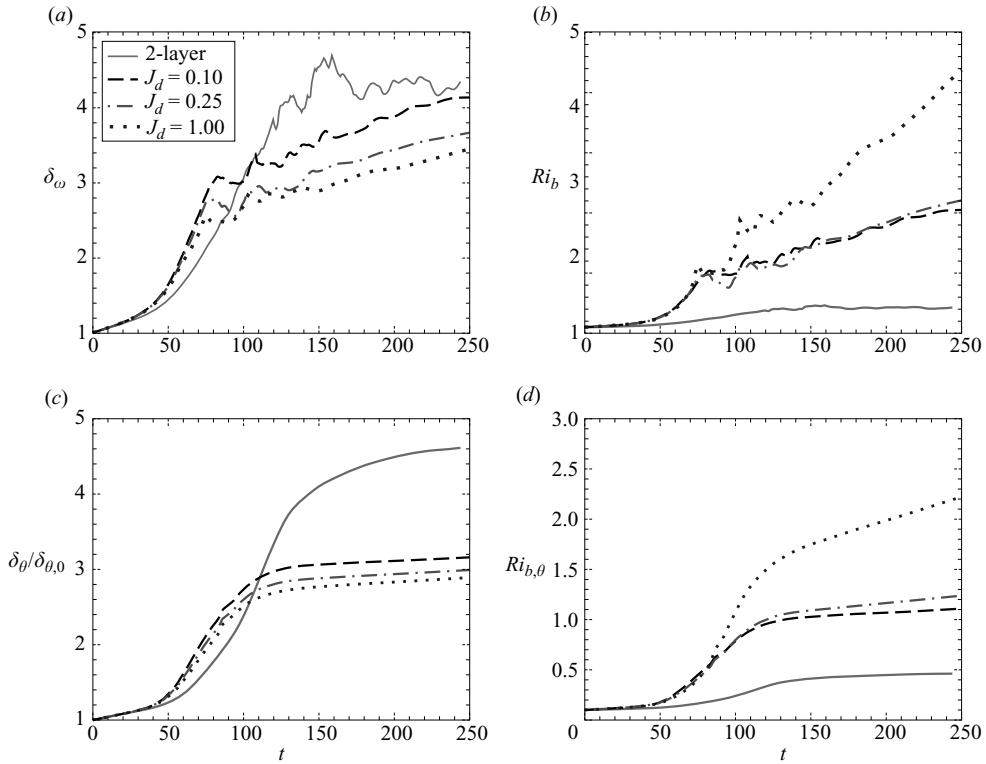
FIGURE 2. (*a*) Vorticity thickness δ_ω. (*b*) Bulk Richardson number Ri_b. (*c*) Momentum thickness δ_θ. (*d*) Bulk Richardson number $Ri_{b,\theta}$.

of the deep stratification on the flow statistics starting with overall quantities: the thickness of the shear layer and the bulk Richardson number Ri_b followed by an account of how the mean profiles develop in time.

Figure 2(*a*) shows the evolution of the vorticity thickness $\delta_\omega(t) = 1/(\mathrm{d}\langle u\rangle/\mathrm{d}z)_{max}$, a typically used measure of the thickness of the sheared region while figure 2(*b*) shows the evolution of the bulk Richardson number defined by

$$Ri_b(t) = \frac{g^* \Delta\rho^*(t)\delta_\omega^*(t)}{\rho_0^* \Delta U^{*2}} = \frac{g\Delta\rho_0^*}{\rho_0^*}\Delta\rho(t)\delta_\omega(t), \qquad (3.1)$$

where $\Delta\rho(t)$ is the density difference across $z = -\delta_\omega(t)$ and $z = \delta_\omega(t)$. Figure 2(*a*) shows that the thickness growth rate is initially smaller in the two-layer case since the value of centreline Richardson number, $J(0) = 0.1$, is larger than the corresponding value of $J(0) = 0.05$ in the cases with deep stratification. The thickness evolves in three different stages. The stage from $t = 0$ to 30 is not a focus of the discussion since the evolution of the shear layer during this period is identical in all cases. After this initial period, there is a second stage where visualization of the vorticity field shows the formation of distinct and dominant KH rollers which increase in size by pairing or amalgamation. We denote this period as the KH regime. Later, when rollers break down, the shear layer enters a third regime, turbulence, wherein small-scale three-dimensional features dominate the vorticity field. The transition time between the second and third regimes is different among cases. In the two-layer case, the transition time occurs late at $t = 130$ while it is earlier, approximately $t = 100$, in J_d

cases. To ease the discussion, from this point we indicate $t = 100$ as the transitional time for all J_d cases. This is the time when the vorticity thickness exhibits a small reduction in size before the growth rate increases due to turbulent stirring. In the KH regime, the vorticity thickness δ_ω grows at slightly higher rate in the J_d cases than in the two-layer case. The growth rate $\mathrm{d}\delta_\omega/\mathrm{d}t$ is 0.045 in the J_d cases and 0.036 in the two-layer case.

In the turbulent regime, there is the following qualitative difference between the two-layer case and the cases with ambient stratification: the shear region in the former approaches an approximately constant thickness while the shear region continues to grow in the latter, see figure 2(a). The asymptotic thickness in the two-layer case corresponds to $Ri_b \simeq 0.38$, a value within the range measured in previous numerical and experimental studies as reviewed by Smyth & Moum (2000a). In the J_d cases, there is a secondary growth that is linear as in the KH regime but at a more moderate rate, approximately $\mathrm{d}\delta_\omega/\mathrm{d}t = 0.004$, with little variation among the different J_d cases. Viscous growth is not the primary cause since a laminar shear layer whose thickness is proportional to $\sqrt{t/Re}$ does not grow linearly and the numerical value of the viscous growth rate is smaller than the observed value. The secondary growth in the turbulence regime strongly influences the evolution of the bulk Richardson number Ri_b as shown in figure 2(b). Ri_b grows vigorously in case $J_d = 1.0$ showing a strong effect of the deep stratification. In all cases the velocity difference does not vary with time so that, according to (3.1), a growth in the thickness δ_ω or in $\Delta\rho$ can cause the observed growth in Ri_b. Case $J_d = 0.10$ has a larger thickness than case $J_d = 1.0$; however, it is the *latter* that has the larger value of Ri_b, nearly twice the corresponding value in the former case. The difference is entirely due to a stronger density gradient across the layer. Thus, the small thickness growth at late time, amplified by a strong external density gradient, results in substantial growth in Ri_b.

Another measure of shear layer thickness is the momentum thickness δ_θ defined by

$$\delta_\theta = \int_{z_l}^{z_u} \left(\frac{1}{4} - \langle u \rangle^2 \right) \, \mathrm{d}z. \tag{3.2}$$

Depths z_u and z_l are upper and lower bounds of the shear layer where the turbulence production is approximately zero but the Reynolds shear stress $\langle u'w' \rangle$ is not necessarily zero. Compare figure 2(a) to figure 2(c), the evolution of δ_ω and δ_θ are similar in the two-layer case, but the J_d cases show strong difference. The secondary growth that was exhibited by δ_ω is much smaller in δ_θ. An analogue of $Ri_b(t)$ is $Ri_{b,\theta}(t)$ obtained by substituting $\delta_\omega(t)$ on the right-hand side of (3.1) by $4\delta_\theta(t)$ and letting $\Delta\rho(t)$ be the density change over $4\delta_\theta(t)$. The factor of 4 ensures that Ri_b and $Ri_{b,\theta}$ have the same value for a tangent-hyperbolic velocity profile. Figure 2(d) shows the evolution of $Ri_{b,\theta}(t)$. Similarly to Ri_b, the quantity $Ri_{b,\theta}$ continues to grow at late time but at a significantly smaller rate. Here, the small but non-zero secondary growth, barely visible in the evolution of δ_θ, is magnified by the density difference across the shear layer.

As the shear layer evolves in time, pycnoclines (regions with large N) are observed at the edges of the layer. The development of an overshoot in density gradient is shown with profiles of non-dimensional squared buoyancy frequency N^2 in figure 3(a, b). The pycnoclines begin to form as soon as the shear layer starts stirring the ambient stratification profile. At first, the formation is similar at both edges. Later, the pycnocline at the bottom edge merges into the strong background density gradient in the bottom region, while the one at the top persists for a long period of time. The density gradient in the pycnocline is unsteady, growing at first, and then decaying due
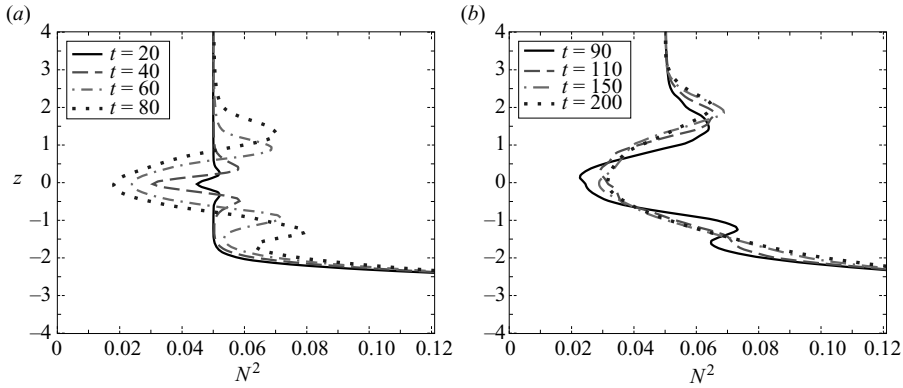
FIGURE 3. Profiles of squared buoyancy frequency N^2 for $J_d = 0.25$ (a) in KH regime, (b) in turbulence regime.
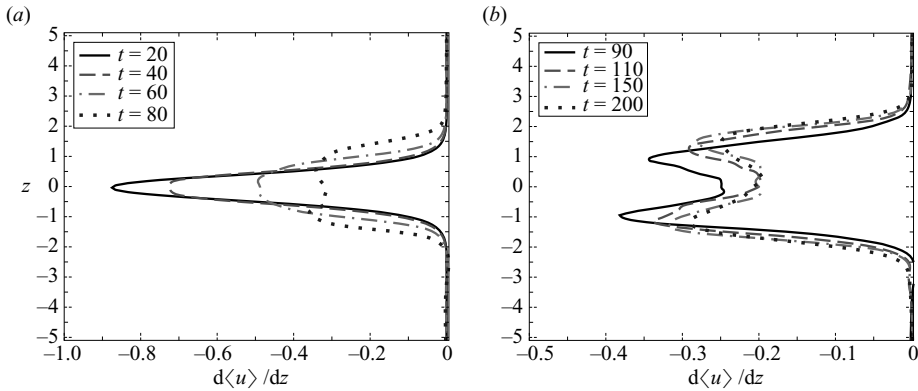

FIGURE 4. Mean shear profiles in case $J_d = 0.25$ (a) in KH regime, (b) in turbulence regime.

to the buoyancy-induced reduction in vertical mixing. The formation of a pycnocline, a result of the mixing of a density gradient by inhomogeneous turbulence, has been observed in previous studies (Linden 1975; Sutherland & Linden 1998; Taylor & Sarkar 2007). The evolution of the mean shear is plotted in figure 4. The evolution during the initial period, $t < 60$, is typical of a shear layer, namely, the profile thickens and the peak shear at $z = 0$ diminishes. However, as shown in figure 4(b), later the mean shear develops local peaks at the upper and lower flanks. The reason is that the enhanced values of N^2 (pycnoclines) at the flanks inhibit the mixing of momentum relative to the centre of the shear layer allowing mean shear at the flanks to be larger than at the centreline. The bottom peak of mean shear is reminiscent of the elevated shear seen at the base of the mixed layer in observations of the transition layer in the upper ocean (D'Asaro *et al.* 1995; Weller & Plueddemann 1996; Johnston & Rudnick submitted).

The gradient Richardson number $Ri_g(z) = N^2/(\mathrm{d}\langle u \rangle/\mathrm{d}z)^2$ is plotted at several times for case $J_d = 0.25$ in figure 5. The profiles of N^2 and $\mathrm{d}\langle u \rangle/\mathrm{d}z$ were earlier shown in figures 3 and 4, respectively. The double hump in the velocity gradient profile is also seen in the Ri_g profile at late times. The late-time behaviour of the gradient Richardson number is governed by the velocity gradients. The downward shift of the shear peak can lead to a reduction in the gradient Richardson number at the edges of
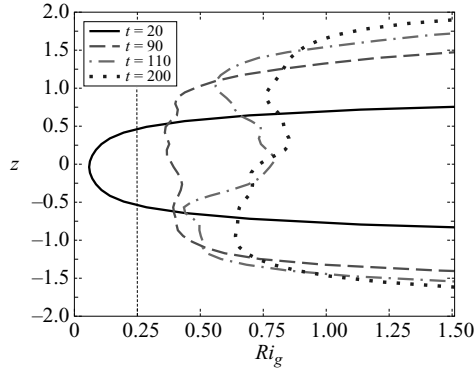
FIGURE 5. Gradient Richardson number Ri_g profiles in case $J_d = 0.25$.

the shear layer at late times. In ocean and atmospheric models, the turbulent mass and momentum transport are typically parameterized in terms of the gradient Richardson number. Specifically, the mixing of mass and momentum due to turbulence is set to zero once the gradient Richardson number reaches a critical value, usually between 0.25 and 1.0. When this type of parameterization is utilized, the shear layer can no longer grow. The spatial profiles of $\mathrm{d}\langle u \rangle / \mathrm{d}z$ and N^2 and hence Ri_g are fixed. By fixing these spatial profiles the secondary (late-time) growth seen in Ri_b (figure 2b) would be missed as would be the late-time evolution of $Ri_g(z)$.

4. Visualization of the shear layer evolution

Visualizations of the spanwise vorticity and the full density field for the two-layer and $J_d = 0.25$ cases illustrate the strong effect of deep stratification on the evolution of the shear layer. Comparisons are also made to the stratified two-layer case of Koop & Browand (1979) and Smyth & Moum (2000a,b).

The spanwise vorticity in the two-layer case on the plane $y = 8.5$ at $t = 70$, 100, 120 and 160 are shown in figure 6(a–d), respectively. At $t = 70$ the roll-up is just beginning, and by $t = 100$ there is evidence of pairing. At $t = 120$ the pairing has completed and the vortices start to break down into small-scale turbulence. Finally, at $t = 160$ there is little evidence of large-scale vortical structures, which have been replaced with a largely disordered field of turbulent motion with smaller length scale. The visualizations presented here are qualitatively similar to the computations of Smyth & Moum (2000a), and to the spatially evolving shear layer studied by Koop & Browand (1979). The roll-up, pairing and breakdown phases in the x–z plane look very similar to those in Koop & Browand (1979). The coherence in the braid region visualized in the x–y plane, not shown, also shows good qualitative agreement with their study.

The evolution of the spanwise vorticity for the $J_d = 0.25$ case is shown in figure 7(a–d) at similar times to those in the two-layer case. In figure 7(a) there is already evidence of smaller scale disorder, $x \approx 38$. Figure 7(b) shows no evidence of pairing, but rather a breakdown, not seen until much later in the two-layer case. The vorticity in figure 7(b) looks more similar to figure 6(c) rather than figure 6(b). The edges of the layer containing significant vorticity in the $J_d = 0.25$ case remain much flatter, with respect to z, than those in the two-layer case. Clearly, the presence of the lower stratification leads to significantly different vertical structure than the one in the
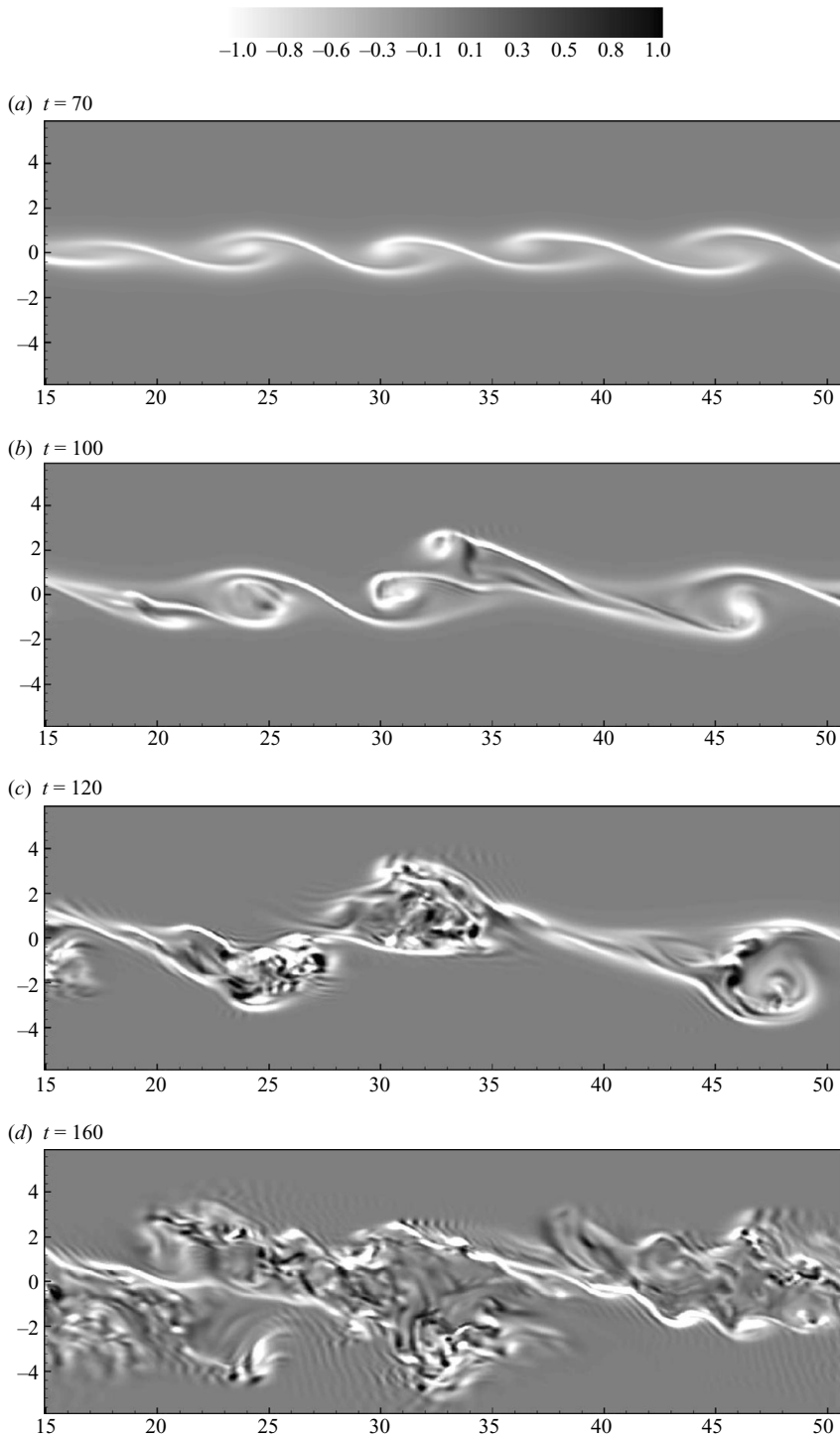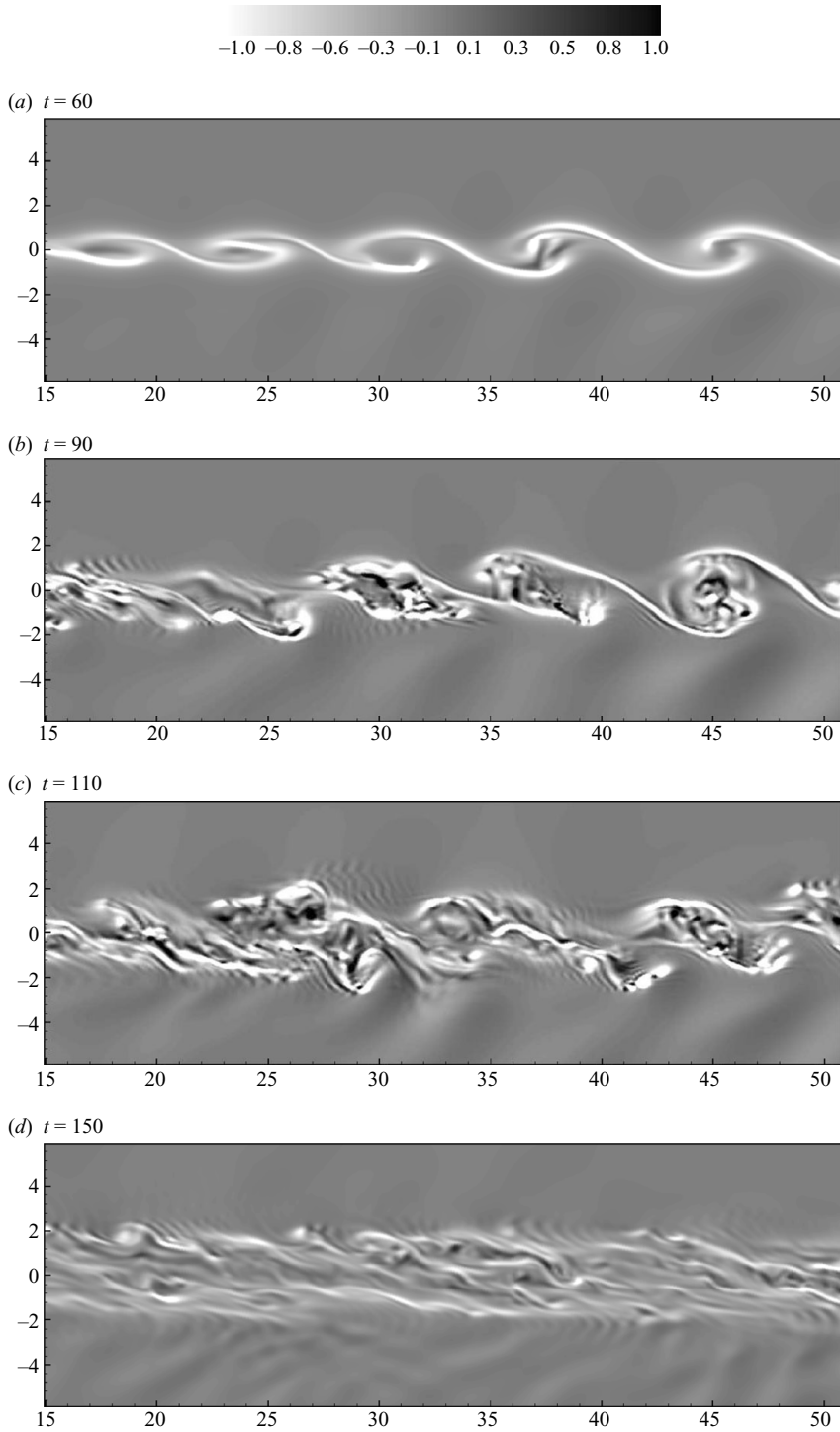
−1.0 −0.8 −0.6 −0.3 −0.1 0.1 0.3 0.5 0.8 1.0

(*a*) *t* = 70

(*b*) *t* = 100

(*c*) *t* = 120

(*d*) *t* = 160

FIGURE 6. Spanwise vorticity ω_2 in x–z plane at $y = 8.5$ in two-layer case.

H. T. Pham, S. Sarkar and K. A. Brucker

-1.0 -0.8 -0.6 -0.3 -0.1 0.1 0.3 0.5 0.8 1.0

(*a*) *t* = 60

(*b*) *t* = 90

(*c*) *t* = 110

(*d*) *t* = 150

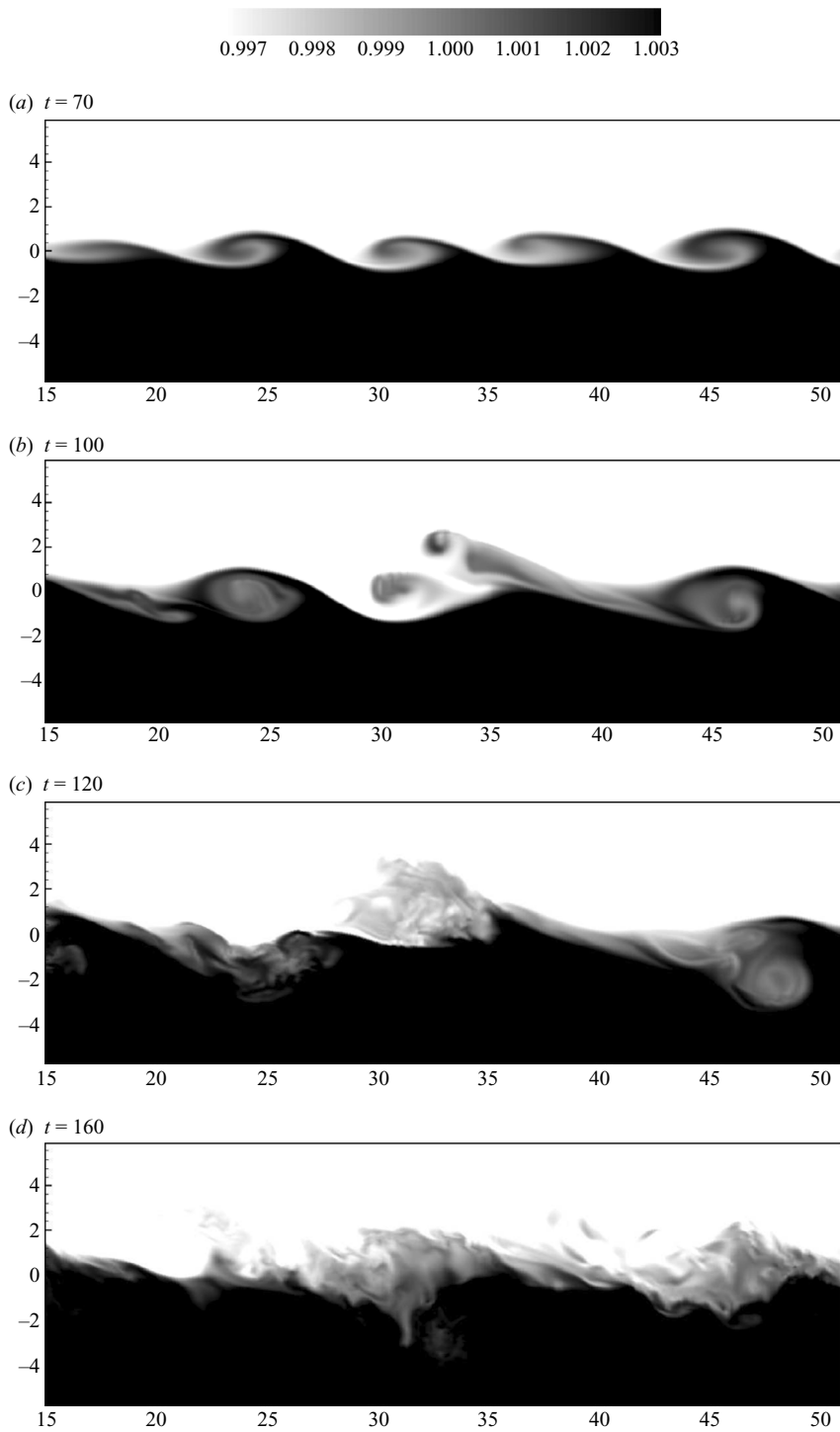FIGURE 7. Spanwise vorticity ω_2 in x–z plane at $y = 8.5$ in case $J_d = 0.25$.

two-layer case. The explanation is as follows: Since the fundamental frequency of the most unstable mode, by linear theory, is affected little by the presence of the deep stratification (Drazin, Zaturska & Banks 1979) the difference must be in the nonlinear portion of the evolution. The first nonlinear process to occur in the two-layer case is pairing. As noted above pairing is evident in figure 6(*b*) and has been disrupted in figure 7(*b*). This lack of pairing was also observed by Strang & Fernando (2001) who were investigating the upper limit of KH formation in terms of the bulk Richardson number. Their stratification was so strong as to eventually suppress the formation of KH rollers. Here, the rollers form but are unable to pair because the lower fluid is too heavy to be displaced above the upper fluid. Like the two-layer case, the thin braid-like regions extend throughout the entire spanwise domain until the rollers begin to breakdown at which time the spanwise coherence is lost.

The density field provides a perspective on mixing by the flow instabilities and turbulence. The full density field is visualized for the two-layer and $J_d = 0.25$ cases in figures 8 and 9, respectively. Figures 8(*a*) and 9(*a*) show the density field in the early stage of KH roller formation. As previously mentioned, the deep stratification has little effect on the disturbance wavelength. However, breakdown to small-scale mixing occurs earlier in the presence of deep stratification. This breakdown is clearly evident at $x \approx 38$ in figure 9(*b*) where regions of mixed fluid have replaced the pairing that occurs in the two-layer case at similar time (figure 8*b*). In figure 8(*b*–*c*) there are regions of mixed fluid that have been completely submersed in regions of higher density, this behaviour is absent in the $J_d = 0.25$ case. The deep stratification prevents the heavy fluid from being lifted above the lighter fluid. At late time the interface between the two fluids is thinner and much smoother in the $J_d = 0.25$ case relative to the two-layer case (compare figure 9*d* to figure 8*d*).

5. Internal wave field

Internal gravity waves that propagate into the stratified region beneath the shear layer are observed during the KH stage in the two cases with $J_d = 0.25$ and 1.0 and, during the later turbulent stage, internal waves are observed in all three cases. The internal wave field is visualized with instantaneous x–z slices of $\partial w'/\partial z$ at various times in figure 10. Since the top region is weakly stratified, $J_s = 0.05$ in all cases, the propagation of internal waves above the shear layer is insignificant. At the base of the shear layer, the phase lines are directed downward and to the left, thus opposing the free stream. The phase lines move upward and, consistent with internal gravity waves, the wave energy moves downward. Phase lines are parallel to the wave group velocity vector, c_g, relative to the bottom free stream velocity. In the present study, c_g transports energy away from the shear region into the bottom deep region.

During the KH regime, waves are excited by KH rollers, analogous to waves excited by flow over a surface corrugation of prescribed wavelength. Let θ be the angle made by the phase lines (equivalently, c_g) with the vertical. Figure 10(*c*, *e*) shows that, in the KH regime, there is a preferred value for θ: 32°–38° when $J_d = 0.25$ and 62°–68° when $J_d = 1.0$. In figure 11, the horizontal wavenumber spectrum at early time, $t = 50$, in the centre of the shear layer shows a strong peak at $k\delta_{\omega,0} = 0.85 \pm 0.06$ which corresponds to $\lambda_{KH} = (7.4 \pm 0.5)\delta_{\omega,0}$, comparable to the wavelength of the most unstable mode $7.2\delta_{\omega,0}$ obtained by linear inviscid theory (Monkewitz & Huerre 1982). (The error bar reported in the wavenumber k is the ratio of π over the sampling period.) The spectrum at depth $z = -2.5\delta_{\omega,0}$, a location at the edge of the shear layer, and at $t = 50$ also shows a peak at the same wavenumber, showing a strong coupling

0.997 0.998 0.999 1.000 1.001 1.002 1.003

(*a*) *t* = 70

(*b*) *t* = 100

(*c*) *t* = 120

(*d*) *t* = 160

FIGURE 8. Density field ρ in x–z plane at $y = 8.5$ in two-layer case.

0.997 0.998 0.999 1.000 1.001 1.002 1.003

(*a*) $t = 60$
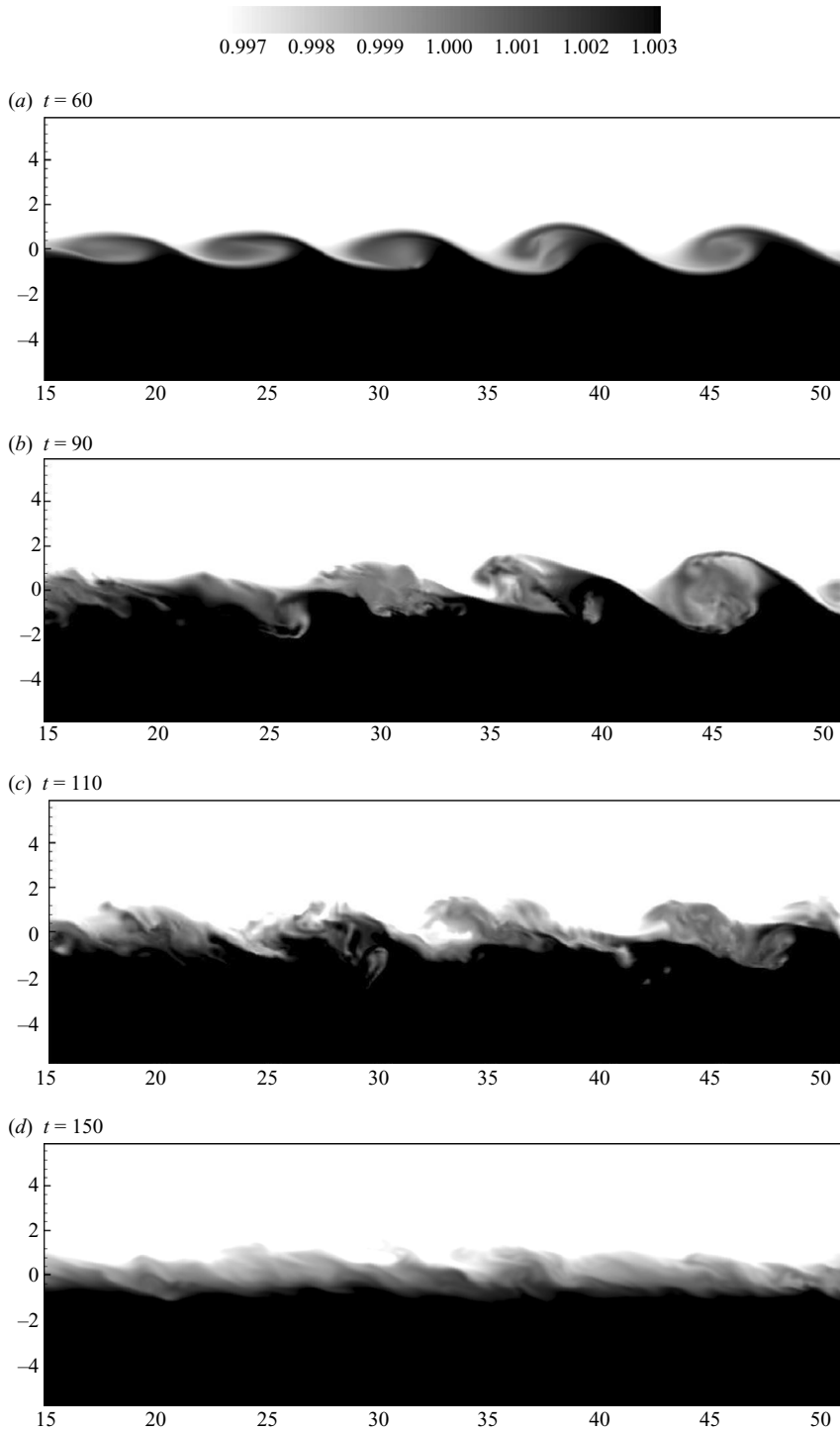
(*b*) $t = 90$

(*c*) $t = 110$

(*d*) $t = 150$

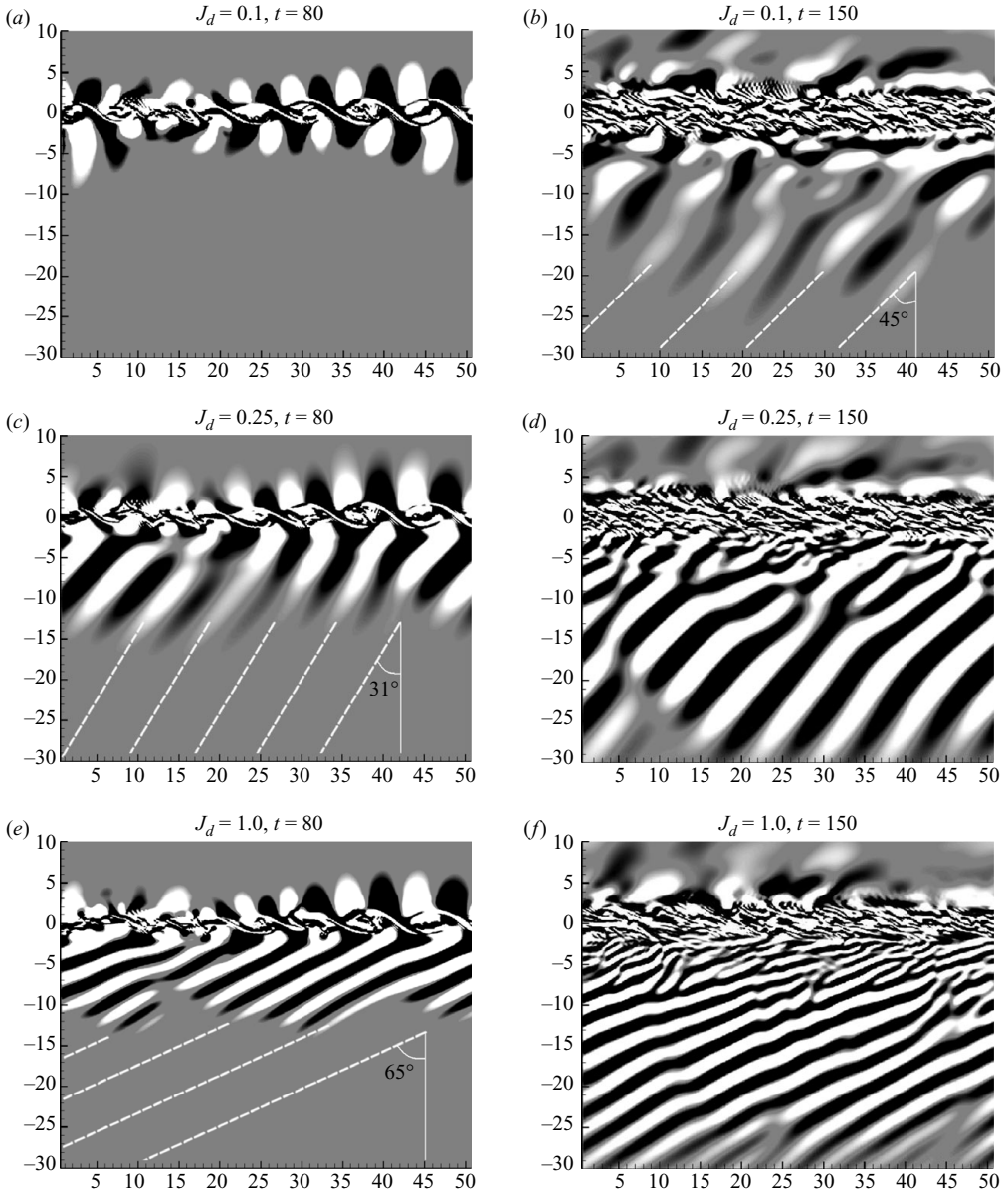FIGURE 9. Density field ρ in x–z plane at $y = 8.5$ in case $J_d = 0.25$.

FIGURE 10. Slices of $\partial w'/\partial z$ in the x–z plane at $y = 8.5$. Strong waves are observed in case $J_d = 0.25$ (c,d) and $J_d = 1.0$ (e,f). The left panels correspond to an early time in the KH regime; the right panels correspond to a later time in the turbulence regime. In the case of $J_d = 0.1$, the internal wave field is negligible in the KH regime (a) but noticeable in the turbulent regime (b). The dashed line in (c,e) shows the propagating angles predicted by linear wave theory. The scale ranges from -0.01 (black) to 0.01 (white).

between the internal waves outside the shear layer and the coherent KH rollers inside the shear layer. Since the rollers are spanwise coherent, the streamwise wavenumber can be considered to represent the horizontal wavenumber for both the rollers and the KH-excited internal waves. The horizontal wavenumber spectra at later time, $t = 100$, are also shown in figure 11. The late-time spectrum inside the shear layer is
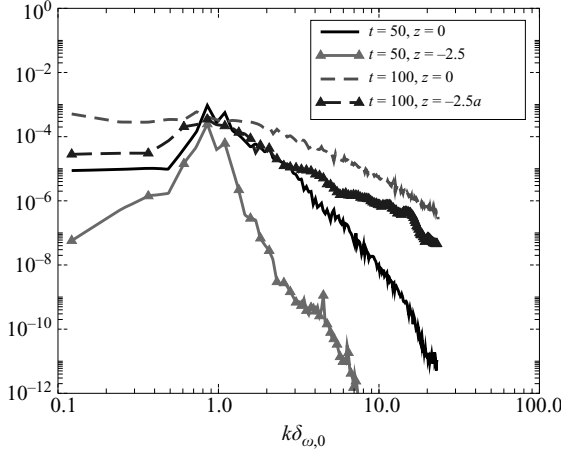
FIGURE 11. Spanwise-averaged power spectra of the vertical velocity on the horizontal centre-plane, $z=0$, and at the bottom edge of the shear layer, $z=-2.5$, in case $J_d=0.25$. Two different times are shown.

broadband *without* a discrete peak at the KH mode. Note that the dependence of the most unstable wavelength on the stratification in the shear layer, J_s, is weak (Hazel 1972) and on the deep stratification is also weak (Drazin *et al.* 1979). Therefore, the wavelength $(7.4 \pm 0.5)\delta_{\omega,0}$ is taken to be representative of all simulated cases.

Linear stability theory that gives the value of the most unstable KH mode in the generation region, combined with linear internal wave theory, can explain the preference for a characteristic angle of the early-time waves shown in figure 10(c, e) as will be demonstrated now. Since the bottom stream moves with a fluid velocity of $0.5\Delta U$, the apparent frequency ω measured in the simulation frame (stationary in this study) is related to the intrinsic frequency Ω measured in the frame moving with the free stream fluid in the bottom region by

$$\omega = \Omega + 0.5\Delta U k. \tag{5.1}$$

The mean streamwise velocity at $z=0$ is $\langle u \rangle = 0$ so that the KH rollers can be approximated to be stationary, i.e. $\omega = 0$, then

$$\Omega = -0.5\Delta U k_{KH} = (0.43 \pm 0.03)\frac{\Delta U}{\delta_{\omega,0}}, \tag{5.2}$$

where k_{KH} is chosen to be negative corresponding to waves propagating in the negative x direction with respect to the bottom free stream.

According to linear theory, internal gravity waves will propagate in a medium if the magnitude of the intrinsic frequency Ω is less than the buoyancy frequency N of that medium. Equation (5.2) then implies that KH-produced internal waves are possible only if the ambient stratification satisfies the following condition:

$$J_d > 0.18. \tag{5.3}$$

Consistent with the above condition, internal waves are not observed during the KH regime in the $J_d=0.10$ case shown in figure 10(a). In contrast, there is strong excitation of internal waves in cases with $J_d=0.25$ and 1.0 as shown in figure 10(c, e). In order to calculate the internal wave phase angle, we combine (5.2) with the linear

dispersion relation for internal gravity waves to obtain,

$$\cos(\theta) = \frac{\Omega}{N} = \frac{0.43 \pm 0.03}{\sqrt{J_d}}. \tag{5.4}$$

According to the prediction of linear theory (5.4) the angle made by the phase lines with the vertical is $\theta = 31° \pm 7°$ when $J_d = 0.25$ and $\theta = 65° \pm 2°$ when $J_d = 1.0$. Figure 10(c, e) shows phase lines with θ in the range of $32°$–$38°$ and $62°$–$68°$ for cases $J_d = 0.25$ and $J_d = 1.0$, respectively. Evidently, there is very good quantitative agreement between the prediction of linear theory and the internal wave angles observed in the present fully nonlinear simulations.

The temporal frequency and wavenumber content of the observed internal waves is further quantified as follows. Part (a) of figures 12–14 shows the time series of $\partial w / \partial z$ measured on a streamwise line located at $y = 8.5$ and $z = -10$ for cases with $J_d = 0.25$, 1.0 and 0.1, respectively. The time series is recorded in the stationary simulation frame. Clearly, the initial wave field during $40 < t < 100$ due to KH rollers is stationary and thus the apparent frequency ω is zero. In part (b) of these figures, the $\partial w / \partial z$ field is mapped into the frame moving at the free stream velocity in the bottom region by

$$x' = x - \langle u \rangle t. \tag{5.5}$$

where $\langle u \rangle$ at this location is close to $0.5 \Delta U$. The power spectra of the mapped field are computed to obtain the intrinsic frequency Ω and the results are shown in part (c) of figures 12–14. Both cases $J_d = 0.25$ and 1.0 show a strong peak at $k\delta_{\omega,0} = 0.85 \pm 0.06$, which is identical to the wavenumber of the most unstable KH mode k_{KH}. The temporal frequency peaks at $\Omega = 0.43 \pm 0.05$ and $(0.41 \pm 0.05) \Delta U / \delta_{\omega,0}$ in case $J_d = 0.25$ and 1.0, respectively. The error bars in the wavenumber and frequency are due to the finite values of spatial length and temporal period in the data that is available to compute the spectra. The diagonal solid line in part (c) of the figures represents the dispersion relation $\Omega = 0.5 \Delta U k$. For cases, $J_d = 0.25$ and 1.0, these diagonal lines pass through the (Ω, k) location of peak power spectrum, and are consistent with the shape of the Ω–k contours. Thus, the computed frequencies agree well with the frequency predicted by linear theory (5.2).

Although the KH rollers cannot excite internal waves in case $J_d = 0.1$ as discussed previously, the thickening of rollers by diffusion and during the pairing process generates disturbances at smaller wavenumber, i.e. larger wavelength such that the radiation condition is met. Figure 14(a) shows the presence of such internal waves. The power spectrum shown in figure 14(c) shows a peak at $k\delta_{\omega,0} = 0.61 \pm 0.06$ and $\Omega = (0.25 \pm 0.06) + \Delta U / \delta_{\omega,0}$, resulting in $\theta = 38° \pm 18°$. The dispersion relation also holds in this case. The solid line slightly deviates from the peak location because the wave packets have a small positive x-velocity in the stationary frame as shown in figure 14(a).

At later time, in the turbulence regime, internal waves continue to be generated by the shear layer. However, as shown by the right panels of figure 10, the phase lines in the vicinity of the shear layer become less structured and the amplitudes are smaller compared to those generated by the rollers. Since the turbulence has a broadband spectrum, turbulence-generated waves are excited over a broad range of angles as shown in figure 10(b, d, f) in the region beneath the shear layer. The wavenumber spectrum, earlier shown in figure 11, indicates that late-time fluctuations are broadband without a discrete peak at the fundamental KH mode. Turbulence-generated internal waves are often observed to eventually propagate at
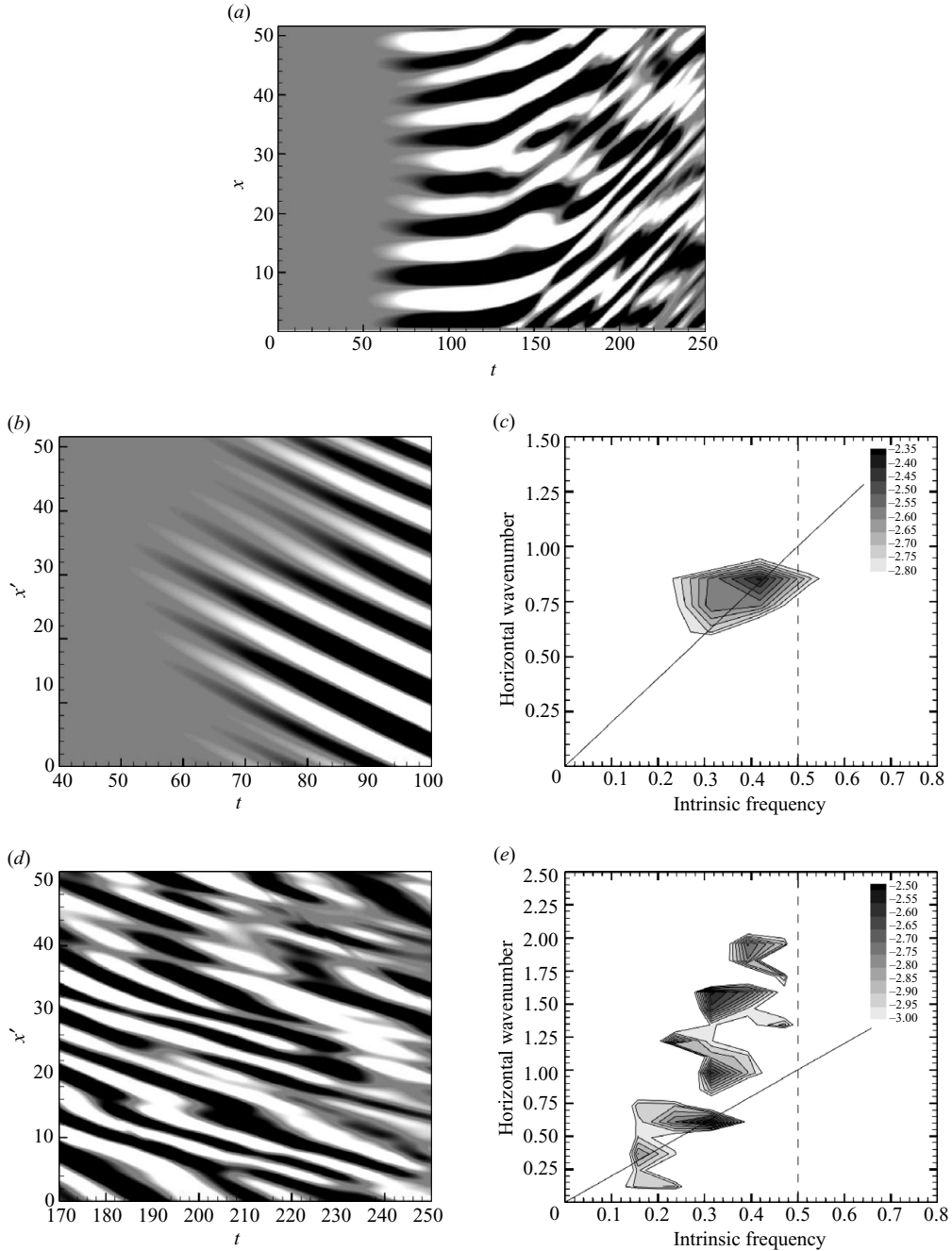
FIGURE 12. Case $J_d = 0.25$: (a) Time series of $\partial w/\partial z$ field at a streamwise line, $z = -10$, $y = 8.5$, in the stationary laboratory frame; (b) the wave field in (a) limited to the duration of the KH regime and mapped to a frame moving with the bottom free stream velocity; (c) power spectrum of the field shown in (b); (d) similar to wave field shown in (b) but in the turbulence regime; (e) power spectrum of the field shown in (d). The scale level in (a, b, d) ranges from -0.01 (black) to 0.01 (white). The contour levels in (c, e) are given in log scale. The vertical dashed line in (c, e) indicates the buoyancy frequency; the diagonal solid line shows the dispersion relation $\Omega = (\Delta U/2) k$.
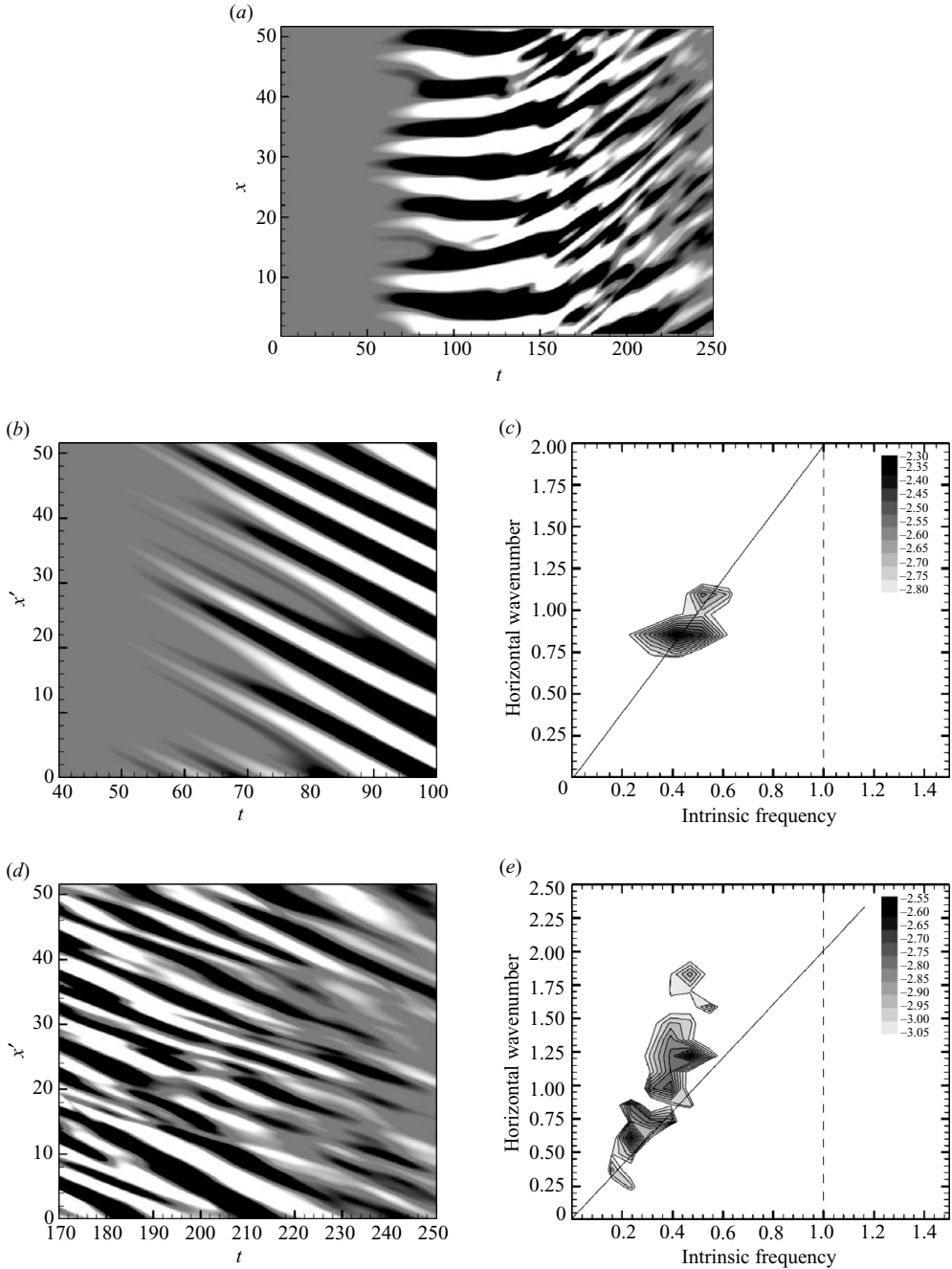
FIGURE 13. Case $J_d = 1.0$: see caption of figure 12.

a narrowband of angles around $\theta = 45°$, although they might span a wide frequency range in the region of generation. The narrowband of propagation angles has been observed in laboratory experiments of a shear layer (Sutherland & Linden 1998) and grid turbulence (Dohan & Sutherland 2003), and in a numerical simulation of a turbulent bottom boundary layer by Taylor & Sarkar (2007). The phase lines of the
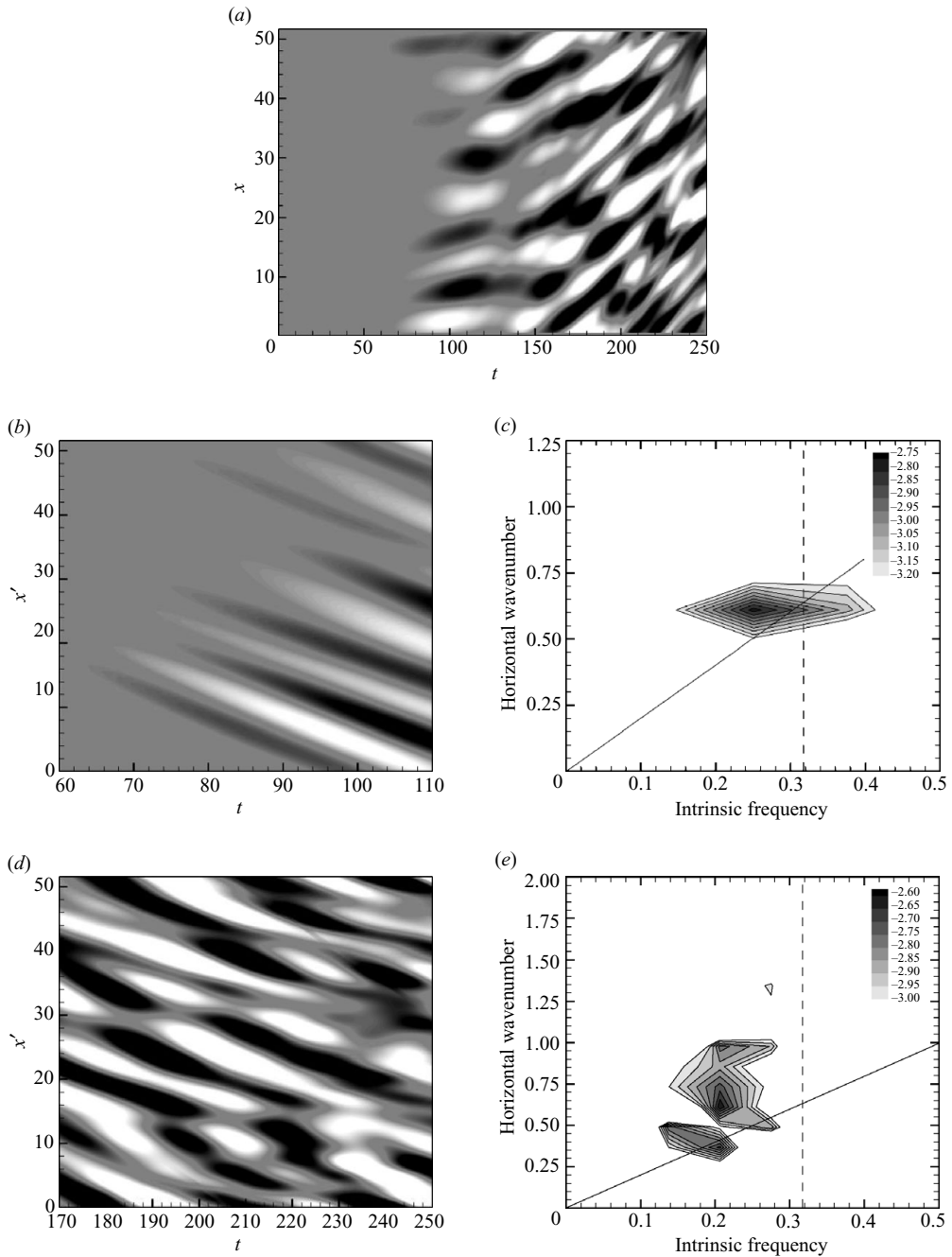
FIGURE 14. Case $J_d = 0.1$: see caption of figure 12.

turbulence-generated waves observed at later time in the $J_d = 0.1$ case also cluster around 45° in the deep region, as shown by figure 10(b). Taylor & Sarkar (2007) offer the following explanation for their boundary-layer-generated waves that is based on frequency-specific viscous decay: both, high- and low-frequency waves, have low
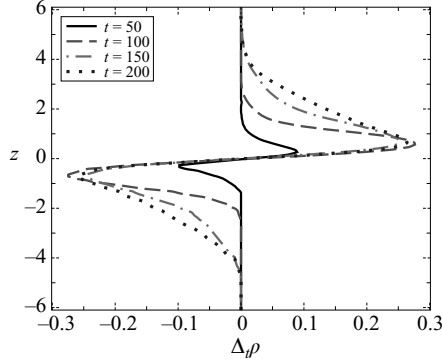
FIGURE 15. Density variation $\Delta_t \rho$ defined in (6.2), in two-layer case.

vertical group velocity, larger time of flight to a given vertical level and large viscous attenuation leaving behind mid-frequency waves clustered around $\theta = 45°$.

Part (e) of figures 12–14 gives the power spectra of the late-time internal waves in a frame moving with the free stream velocity. The peak intrinsic frequencies in cases $J_d = 0.1$, 0.25 and 1.0 are 0.21 ± 0.04, 0.31 ± 0.04 and $(0.47 \pm 0.04)\Delta U/\delta_{\omega,0}$, which correspond to $\theta = 48° \pm 10°$, $52° \pm 6°$ and $62° \pm 3°$, respectively. The range of wavenumbers in the power spectra is broader than the early-time spectra in part (c) of these figures. Furthermore, the solid diagonal line, $\Omega = (\Delta U/2)k$ is not consistent with the observed power spectrum, showing that the theory that was demonstrated for the KH-generated waves does not work for the late-time turbulence-generated waves.

6. Mass transport

Linear wave theory predicts that there is no net mass transport by internal waves over a wave period; however, we observe an accumulation of mass in the region near the shear layer. We will show below that the observed mass gain is due to molecular diffusion. The density gradient at the bottom is more negative than at the top surface resulting in an accumulation of mass in the shear layer.

Take the horizontal average of the density equation (2.3),

$$\frac{\partial \langle \rho \rangle}{\partial t} = -\frac{\partial \langle \rho' w' \rangle}{\partial z} + \frac{1}{Re_0 Pr} \frac{\partial^2 \langle \rho \rangle}{\partial z^2}, \tag{6.1}$$

where $\langle \cdot \rangle$ denotes average quantity. The density change in time $\Delta_t \rho$ can be defined by

$$\Delta_t \rho = \langle \rho \rangle(z, t) - \langle \rho \rangle(z, t = 0), \tag{6.2}$$

and the net mass accumulation $\Delta_t m$ is the spatial integral of $\Delta_t \rho$ from $z = z_l$ to z_u. The depths z_l and z_u are chosen away from the shear layer where the mean density gradient does not vary in time. Integration of (6.1) in space and time results in

$$\Delta_t m = \int_{z_l}^{z_u} \Delta_t \rho \, \mathrm{d}z = \int_0^t \langle \rho' w' \rangle(z_l) \, \mathrm{d}t + \frac{1}{Re_0 Pr} \frac{\Delta U^2}{g\delta_{\omega,0}}(J_d - J_s)t, \tag{6.3}$$

where the vertical mass flux $\langle \rho' w' \rangle$ at z_u is negligible. The left-hand side of (6.3) gives the net mass gain $\Delta_t m$ in the shear layer. Figure 15 shows profiles of $\Delta_t \rho$ at various times in the two-layer case. As the shear layer evolves, the upper portion gets heavier
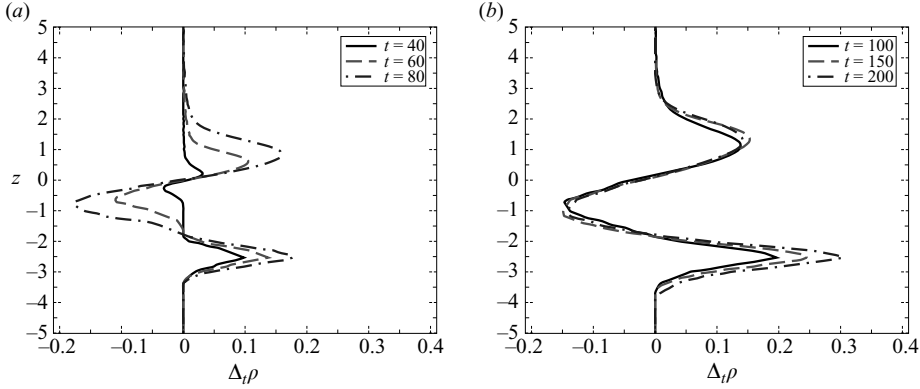
FIGURE 16. Density variation, $\Delta_t \rho$ defined in (6.2), in case $J_d = 0.25$ (*a*) in KH regime, (*b*) in turbulence regime.

while the lower portion gets lighter as a result of mixing. The spatial integration of any of the profiles in this figure, i.e. the left-hand side of (6.3), yields zero mass gain. This agrees with the right-hand side since there is neither mass flux $\langle \rho' w' \rangle$ nor density gradient outside the shear region in the two-layer case.

In the J_d cases, the mixing in the shear layer is similar but there is an accumulation of mass in the transition region where J_s merges with J_d. Figure 16(*a*) shows the density variation profiles in case $J_d = 0.25$ during the KH regime. The figure shows density variation $\Delta_t \rho$ due to shear mixing around the shear centre $z = 0$ accompanied by variation due to viscous diffusion in the transition region around $z = -2.5$. At $t = 40$, the variation due to diffusion is larger than that due to shear mixing. As the shear layer evolves, the mixing region thickens until it reaches the transition region. The growth of the mixing region is restrained by the presence of the transition region when compared to the two-layer case. The transition region exhibits insignificant thickness growth in time. In the turbulence regime, as shown in figure 16(*b*), the mixing due to shear becomes steady but the viscous mass diffusion into the transition region continues. The density variation due to diffusion outgrows the effect of mixing at late time. It is noted that, according to the diffusive term in (6.3), the region of maximum accumulation has the largest difference in density gradient across the region. Thus, the transition region indeed shows the maximum density variation.

According to linear wave theory, internal waves do not transport mass, i.e. the integration of vertical mass flux $\langle \rho' w' \rangle$ over a wave period is zero. Figure 17(*a*) shows the time evolution of the mass flux across depth $z = -5$ in the J_d cases. The profiles show an upward flux trailed by a downward flux. However, the upward flux is stronger than the downward resulting in a net upward flux. The imbalance is due to the unsteady decaying source in the shear layer. Although there is a mass transport due to internal waves, the gain is small relative to the diffusive mass accumulation as shown in figure 17(*b*). In the figure, the dots represent the net mass gain in the shear layer $\Delta_t m$ calculated using the right-hand side of (6.3). The dashed line shows the gain due to solely the diffusive term on the right-hand side. In the computation, we take $z_l = -5$ and $z_u = 5$ where the density gradient does not vary in time. It is obvious that the mass accumulation inside the shear layer is mainly contributed by diffusion. The effect from the internal waves during the period $t = 60$–130 when the wave flux $\langle \rho' w' \rangle$ is strong leads to no net mass gain.
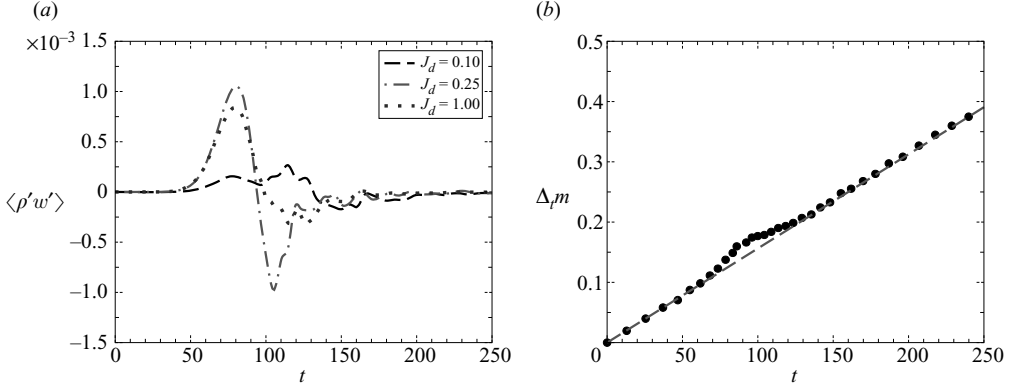
FIGURE 17. (*a*) Vertical mass fluxes at $z = -5$. (*b*) Net mass gain inside the shear layer in case $J_d = 0.25$. The dots show the net mass gain in the shear layer. The dashed line denotes the diffusive contribution.
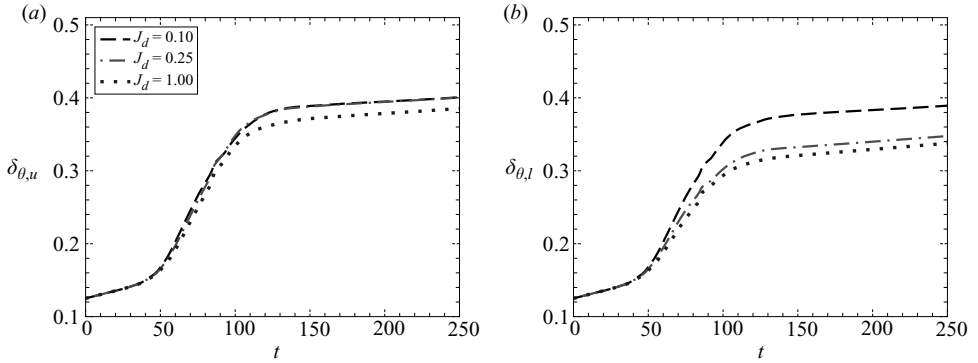

FIGURE 18. Momentum thickness: (*a*) upper portion $\delta_{\theta,u}$, (*b*) lower portion $\delta_{\theta,l}$.

7. Momentum transport

Internal waves provide a viable route for momentum transport from a region with instabilities and turbulence to an external quiescent region. In order to quantify the momentum loss due to wave excitation, we examine the evolution of the momentum thickness of the shear layer. The momentum thickness δ_θ was defined previously by (3.2). Since the stratification in the top and bottom regions is different, (3.2) is split into upper and lower portions,

$$\delta_\theta = \delta_{\theta,u} + \delta_{\theta,l} = \int_{z_l}^{z_0} \left(\frac{1}{4} - \langle u \rangle^2 \right) \mathrm{d}z + \int_{z_0}^{z_u} \left(\frac{1}{4} - \langle u \rangle^2 \right) \mathrm{d}z, \tag{7.1}$$

where z_0 is the location of zero velocity. Figure 18(*a*, *b*) shows the time evolution of the momentum thickness in the upper and lower portions, respectively. It is evident that the shear layer grows asymmetrically. The asymmetry is related to the stratification intensity in the deep layer. In case $J_d = 0.10$, the upper and lower portions grow similarly. When J_d increases, the lower portion grows significantly less. In case $J_d = 0.25$ where strong internal waves are observed in the bottom region, the top portion grows *exactly* as in case $J_d = 0.10$. However, the bottom portion is nearly 15 % smaller. Comparing case $J_d = 1.0$ to case $J_d = 0.25$, it is observed

that the thickness growth is less in both upper and lower portions. Stratification decreases overall turbulence production in the core of the shear layer but enhances Reynolds shear stress at the boundaries by allowing internal waves. In order to distinguish between these two features, it is necessary to make precise the quantities that contribute to the thickness growth. Differentiating each portion of (7.1) in time yields

$$
\frac{\mathrm{d}\delta_{\theta,u}}{\mathrm{d}t} = -\int_{z_0}^{z_u} \frac{\mathrm{d}\langle u\rangle^2}{\mathrm{d}t}\,\mathrm{d}z,
$$
$$
\frac{\mathrm{d}\delta_{\theta,l}}{\mathrm{d}t} = -\int_{z_l}^{z_0} \frac{\mathrm{d}\langle u\rangle^2}{\mathrm{d}t}\,\mathrm{d}z.
$$
(7.2)

When the x-component of the momentum equation is averaged in the horizontal directions and the result is multiplied with the mean velocity $\langle u\rangle$, we obtain

$$
\frac{1}{2}\frac{\mathrm{d}\langle u\rangle^2}{\mathrm{d}t} = \langle u'w'\rangle\frac{\mathrm{d}\langle u\rangle}{\mathrm{d}z} - \frac{\mathrm{d}}{\mathrm{d}z}[\langle u\rangle\langle u'w'\rangle] - \frac{1}{Re_0}\left(\frac{\mathrm{d}\langle u\rangle}{\mathrm{d}z}\right)^2 + \frac{1}{Re_0}\frac{\mathrm{d}}{\mathrm{d}z}\left[\langle u\rangle\frac{\mathrm{d}\langle u\rangle}{\mathrm{d}z}\right]. \quad (7.3)
$$

Substitution of the above result into (7.2) leads to the following expression for the temporal rate of change of momentum thickness:

$$
\frac{\mathrm{d}\delta_{\theta,u}}{\mathrm{d}t} = 2\int_{z_0}^{z_u}\left[P + \frac{1}{Re}\left(\frac{\mathrm{d}\langle u\rangle}{\mathrm{d}z}\right)^2\right]\mathrm{d}z - \langle u'w'\rangle(z=z_u),
$$
$$
\frac{\mathrm{d}\delta_{\theta,l}}{\mathrm{d}t} = 2\int_{z_l}^{z_0}\left[P + \frac{1}{Re}\left(\frac{\mathrm{d}\langle u\rangle}{\mathrm{d}z}\right)^2\right]\mathrm{d}z - \langle u'w'\rangle(z=z_l).
$$
(7.4)

Here, $P = -\langle u'w'\rangle(\mathrm{d}\langle u\rangle/\mathrm{d}z)$ is the turbulence production. We have used the conditions that $\langle u\rangle = -1/2, 0, 1/2$ at $z=z_u, 0, z_l$, respectively. The last terms in (7.3) can be ignored since the velocity gradient at depths z_u and z_l is relatively small. Integrating (7.4) from time t_0 to t, the expression for momentum thickness as a function of time takes the form

$$
\delta_{\theta,u}(t) = \delta_{\theta,u}(t_0) + 2\int_{t_0}^{t}\int_{z_0}^{z_u}\left[P + \frac{1}{Re_0}\left(\frac{\mathrm{d}\langle u\rangle}{\mathrm{d}z}\right)^2\right]\mathrm{d}z\,\mathrm{d}t - \int_{t_0}^{t}\langle u'w'\rangle(z=z_u)\,\mathrm{d}t,
$$
$$
\delta_{\theta,l}(t) = \delta_{\theta,u}(t_0) + 2\int_{t_0}^{t}\int_{z_l}^{z_0}\left[P + \frac{1}{Re_0}\left(\frac{\mathrm{d}\langle u\rangle}{\mathrm{d}z}\right)^2\right]\mathrm{d}z\,\mathrm{d}t - \int_{t_0}^{t}\langle u'w'\rangle(z=z_l)\,\mathrm{d}t.
$$
(7.5)

The growth of momentum thickness is the result of a positive contribution from the turbulence production in the shear layer and a negative contribution from the momentum flux $\langle u'w'\rangle$ at the edges of the shear layer. The viscous contribution can be neglected at high Reynolds number. Since the stratification is weak in the top region, we focus our discussion on the bottom region where the fluid is strongly stratified. Figure 19(a) shows the time evolution of the momentum flux $\langle u'w'\rangle$ at depth $z_l = -5$ for the three cases. The flux is the strongest in case $J_d = 0.25$, and the weakest in case $J_d = 0.10$. Although, less momentum is transported away in case $J_d = 1.0$ relative to case $J_d = 0.25$, δ_θ is *smaller* in the former. This is a result of the reduction in turbulence production owing to buoyancy. It is of interest to compare the radiated momentum flux in the shear layer with other configurations. The peak value of $\langle u'w'\rangle \simeq 2 \times 10^{-3}$ in figure 19(a) for the internal wave momentum flux is
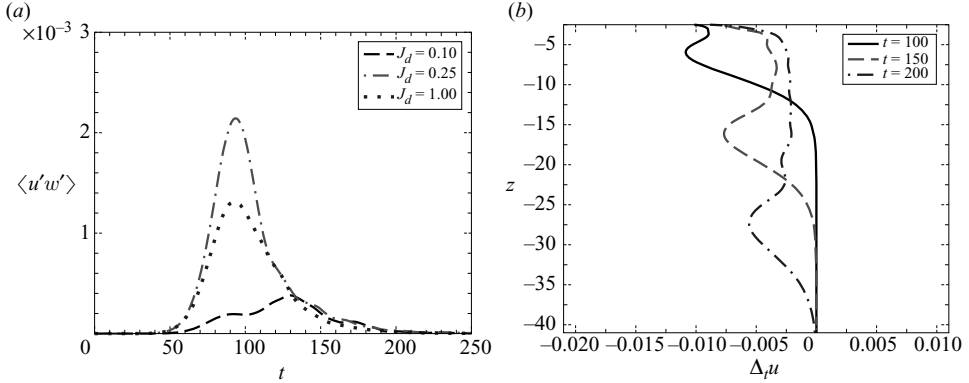
FIGURE 19. (a) Reynolds stress $\langle u'w' \rangle$ at depth $z_l = -5$. (b) Variation in the mean velocity profile, $\Delta_t u$, in case $J_d = 0.25$.

larger than the corresponding value of $\langle u'w' \rangle \leqslant 10^{-4}$ observed in a jet by Smyth & Moum (2002).

In order to estimate the efficiency of momentum transport by internal waves, we compare the time-integrated Reynolds shear stress in (7.6) to the initial momentum in the shear layer, which is 1 ($\Delta U^* \delta^*_{\omega,0}$, dimensionally). The time integration from $t = 0$ to 250 indicates approximately 10 % ($J_d = 0.25$), 7 % ($J_d = 1.0$) and 3 % ($J_d = 0.10$) of the initial momentum can be extracted by the internal waves. In their study of a shear layer formed by flow over a vertical barrier, Sutherland & Linden (1998) report slightly higher values from their two-dimensional simulations. This is typical since velocity fluctuations are more correlated in two-dimensional flows. In their laboratory experiments, 7 % is the maximum value that is observed for the momentum propagated away by the internal waves. As the internal waves propagate downward with significant amount of momentum, the mean flow decelerates as noted by Fritts (1982). Figure 19(b) shows the variation in the mean velocity profile, $\Delta_t u(z,t) = \langle u \rangle (z,t) - \langle u \rangle (z,t=0)$. The deceleration magnitude can be 1 % near the shear layer and reduces to a smaller value as the waves travel away owing to local viscous diffusion.

8. Energy transport

The amount of fluctuation energy transported away from the shear layer by internal waves is quantified and found to be substantial. The shearing event generates fluctuation kinetic energy and waves carry the energy into the deep layer. Therefore, velocity fluctuations measured by the turbulent kinetic energy *tke* denoted by $K = 1/2\langle u'_i u'_i \rangle$, accumulate outside the shear layer. (Although we use the terms turbulent kinetic energy and fluctuation kinetic energy interchangeably, non-zero K well outside the shear layer is wave energy and not turbulence.) The amount of energy transported is obtained by subtracting the amount of energy inside the shear zone from the total amount present in the simulated domain. Integration of K from $z = -\delta_\omega$ to δ_ω provides a good measure of the *tke* inside the shear zone. Figure 20(a, b) shows the spatially integrated K as a function of time for cases $J_d = 0.25$ and 1.0, respectively. The dashed line indicates the energy inside the shear layer and the solid line shows the energy in the test domain that excludes the sponge regions. The difference between the two curves yields the amount of energy transported outside
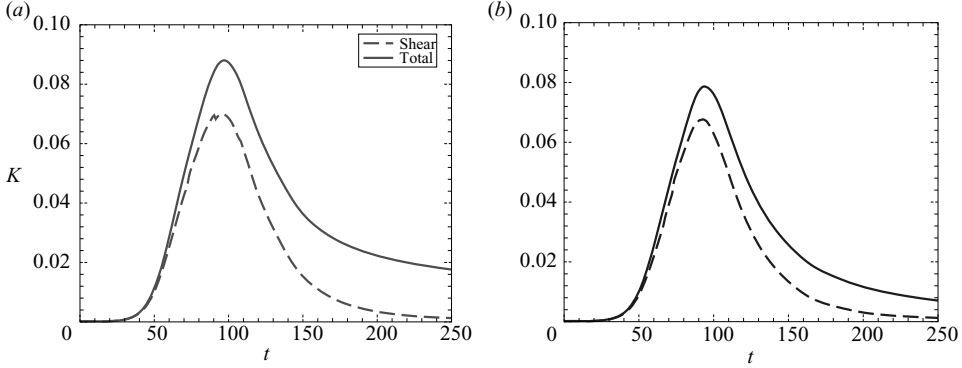
FIGURE 20. Integrated turbulent kinetic energy (*a*) $J_d = 0.25$, (*b*) $J_d = 1.0$; —, over test domain; – – –, over the shear layer.

the layer by the internal waves. Transport to the exterior starts at $t = 50$, shortly after the KH rollers begin to develop. Fluctuation energy associated with instabilities and turbulence progressively builds up inside the shear layer and, correspondingly, more energy is pumped into the deep region below the shear layer. At late time, the energy inside the shear layer vanishes owing to the dissipative nature of turbulence, but energy remains present outside where the viscous dissipation is relatively weak. Outside the shear layer, the energy resides mainly in the bottom region where the ambient stratification supports internal waves. From figure 20(*a*), approximately 0.02 ΔU^2 has been transported (the difference between the two lines at late time). Relative to the initial mean kinetic energy inside the shear layer, the transported energy is roughly 15 % in case $J_d = 0.25$, 7 % in case $J_d = 1.0$ and 3 % in case $J_d = 0.10$. The initial mean kinetic energy is calculated by integrating $1/2\langle u \rangle^2$ at time $t = 0$ from $z = -\delta_{\omega,0}$ to $\delta_{\omega,0}$.

It is desirable to describe the 'efficiency' of energy transport in light of the *tke* budget. The evolution equation for the turbulent kinetic energy is

$$\frac{\mathrm{d}K}{\mathrm{d}t} = P - \varepsilon + B - \frac{\partial T_i}{\partial x_i}. \tag{8.1}$$

Here, K is the turbulent kinetic energy defined previously, P is the production rate, defined as

$$P \equiv -\langle u_i' u_j' \rangle \frac{\partial \langle u_i \rangle}{\partial x_j} = -\langle u'w' \rangle \frac{\mathrm{d}\langle u \rangle}{\mathrm{d}z},$$

ε is the dissipation rate, defined as

$$\varepsilon \equiv \frac{2}{Re_0} \langle s_{ij}' s_{ij}' \rangle \, ; s_{ij}' = \frac{1}{2} \left(\frac{\partial u_i'}{\partial x_j} + \frac{\partial u_j'}{\partial x_i} \right),$$

B is the buoyancy flux, defined as

$$B \equiv -Ri_{b,0} \langle \rho' w' \rangle,$$

$\partial T_i / \partial x_i$ is the transport of *tke*, defined by

$$T_i \equiv \frac{1}{2} \langle u_i' u_j' u_j' \rangle + \langle u_i' p' \rangle - \frac{2}{Re_0} \langle u_j' s_{ij}' \rangle.$$
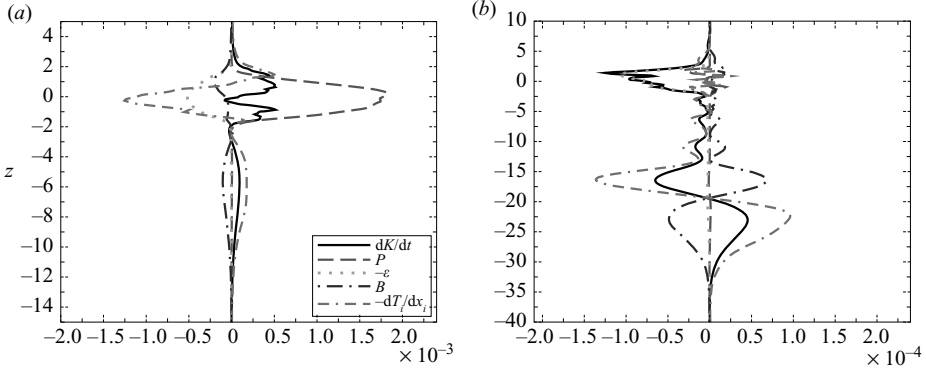
FIGURE 21. Vertical profiles of *tke* budget in case $J_d = 0.25$ at (a) $t = 83$, (b) $t = 160$.

For the present flow, the transport term simplifies to $\partial T_3 / \partial z$ with

$$T_3 = \frac{1}{2}[\langle w'u'u' \rangle + \langle w'v'v' \rangle + \langle w'w'w' \rangle] + \langle p'w' \rangle - \frac{2}{Re_0}[\langle u's'_{31} \rangle + \langle v's'_{32} \rangle + \langle w's'_{33} \rangle].$$

Figure 21(a, b) shows the profile of each term in the *tke* budget in case $J_d = 0.25$ at time $t = 83$ and 160, respectively. At $t = 83$, the production and dissipation are large but restricted to the shear region. The presence of propagating internal waves external to the shear layer is shown by the extension of profiles of the buoyancy flux, transport (essentially $d\langle p'w' \rangle / dz$) and dK/dt into the deep region. At time $t = 160$, the production is negligible and, in the shear region, the dissipation rate is balanced by dK/dt. The internal gravity waves continue to transport energy into the deep region. The profiles at $t = 160$ show that, in the deep region, approximately half of the transport goes into changing the fluctuation kinetic energy and half into the buoyancy flux, i.e. changing the fluctuation potential energy.

We now characterize the energetics of the fluctuations during the entire evolution rather than at the two specific times of figure 21. Integrating (8.1) from depth $z^\star$ to the top boundary z^t_{max} of the test region yields

$$\int_{z^\star}^{z^t_{max}} \frac{dK}{dt} \, dz = \int_{z^\star}^{z^t_{max}} P \, dz - \int_{z^\star}^{z^t_{max}} \epsilon \, dz + \int_{z^\star}^{z^t_{max}} B \, dz + \langle p'w' \rangle(z^\star). \tag{8.2}$$

Figure 22(a) shows the time evolution of terms in (8.2) for case $J_d = 0.25$. The spatial integration includes the upper region excluding the sponge region, the shear layer and the bottom region down to depth $z^\star = -5$. As the vortices roll up, there is significant energy extraction from mean shear by fluctuations through the turbulent production, some of which is used to increase turbulent kinetic energy. Also in the presence of the rollers, the buoyancy flux reaches its maximum value since larger eddies have the capability to lift up heavy fluid. The peak dissipation rate occurs at later time when the flow turns turbulent. The term $\langle p'w' \rangle$, called the pressure transport term in the turbulence literature and the internal wave flux in the literature on waves, is significant and occurs at a time between the occurrence of peak production and peak dissipation. When $z^\star$ is far away from the shear layer, the internal wave (IW) flux $\langle p'w' \rangle$ dominates the other transport terms. Figure 22(b) shows the energy flux $\langle p'w' \rangle$ at $z = -5$ for the three simulated cases. Similar to the momentum flux, the IW flux depends strongly on the stratification in the deep region. For weak stratification ($J_d = 0.1$) the wave excitation is negligible and so is the IW flux. Case $J_d = 0.25$ has
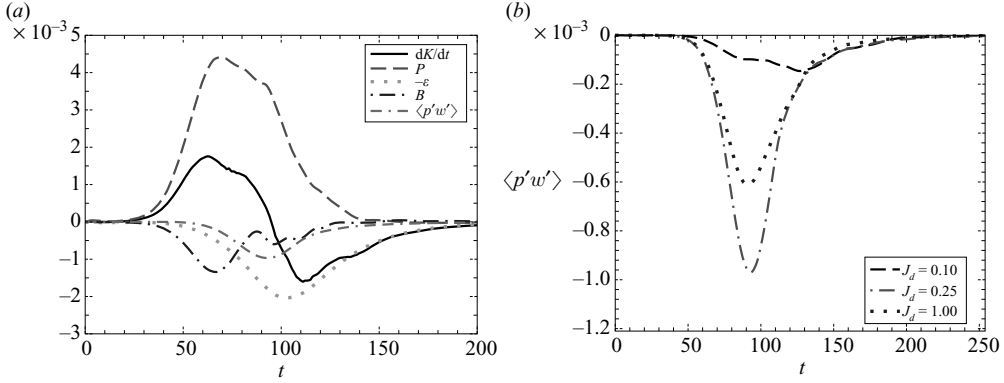
FIGURE 22. (a) Balance of *tke* for $J_d = 0.25$. The production, dissipation and buoyancy flux are integrated from z_{max}^t to $z = -5$. $\langle p'w' \rangle$ is at $z = -5$. (b) Internal wave flux $\langle p'w' \rangle$ at $z = -5$ compared among different cases.

J_d	IW/P	IW/ϵ	$IW/(-B)$	ϵ/P	$(-B)/P$	Γ	Γ_d
0.1	0.05	0.08	0.18	0.6	0.28	0.46	0.46
0.25	0.17	0.33	0.75	0.53	0.23	0.44	0.44
1.0	0.14	0.25	0.57	0.55	0.24	0.44	0.43

TABLE 1. Energy flux efficiency, energy partition and mixing efficiency. The terms in the *tke* budget are integrated in both time and space (from $z = -5$ to z_{max}^t) to calculate the tabulated values.

the strongest IW flux, not $J_d = 1.0$. The dependence of internal wave flux on J_d is non-monotone because increasing the stratification, on one hand, increases the flux for a given amplitude of vertical velocity fluctuation but, on the other hand, decreases the vertical velocity fluctuations in the generation region. In the shear layers simulated here, the net IW flux due to the rollers is significantly higher than the flux due to small-scale turbulence.

An overall quantification of the efficiency of IW flux is obtained by integration of (8.2) from time $t = 0$ to late time t_f when turbulent kinetic energy inside the shear layer vanishes. This procedure is convenient since the temporal peak values of the various terms in the *tke* balance occur at different times. Table 1 shows the efficiency of energy transport by waves relative to other terms in the energy budget. Strang & Fernando (2001) estimate the ratio of IW flux to the rate of change of potential energy as approximately 48 %, slightly smaller than the values of 75 % and 57 % for $IW/(-B)$ in table 1. The production P measures the extraction of *tke* from the mean shear flow by the Reynolds shear stress of the fluctuations. It is useful to quantify the partition of the extracted energy into the various sinks of the *tke* balance as done in columns 2, 5 and 6 of table 1. In case $J_d = 0.25$, 53 % of the production is dissipated, 23 % used for stirring the density field and 17 % is transported away by internal waves. In the same order, the values are 55 %, 24 % and 14 % for case $J_d = 1.0$ and 60 %, 28 % and 5 % for case $J_d = 0.1$. As the numbers show, internal waves can considerably alter the energetics inside the shear layer.

The quantity $\Gamma = -B/\epsilon$ the so-called mixing efficiency is an important quantity that is often used by oceanographers to infer the eddy diffusivity of mass K_ρ from the dissipation rate obtained by microstructure measurements or estimated by measurement of the Thorpe scale. If Γ is known, the expression $K_\rho = \Gamma \epsilon / N^2$ can be used without further approximation to obtain the eddy diffusivity (Osborn 1980). The quantity $\Gamma_d = \epsilon_\rho / \epsilon$ can be measured directly in the ocean from temperature gradient and velocity shear data, and is used as a surrogate for the mixing efficiency (Oakey 1985). Here, ϵ_ρ is defined by

$$\epsilon_\rho = \frac{1}{Pr\,Re_0} \frac{g}{\rho_0 |\mathrm{d}\bar\rho/\mathrm{d}z|} \overline{\frac{\partial \rho'}{\partial x_k} \frac{\partial \rho'}{\partial x_k}}. \tag{8.3}$$

The quantity ϵ_ρ signifies irreversible loss of turbulent potential energy to the background density field. The last two columns of table 1 give the overall mixing efficiency where the buoyancy, viscous and scalar dissipation are integrated in time before the ratios are taken. Although $\Gamma = \Gamma_d = 0.2$ is often employed, the value can depend on the type of flow, the age of the flow in non-stationary examples, as well as other parameters such as Reynolds number, Richardson number and Prandtl number. Here, both Γ and Γ_d are approximately 0.44 for all J_d cases, somewhat smaller than the value of 0.6 reported by Smyth *et al.* (2001) where they simulate a two-layer case at $Re = 1965$ and $Ri_b = 0.08$.

9. Conclusions

The direct numerical simulations conducted here show that the presence of an ambient region with uniform stratification substantially changes the evolution of a stratified shear layer from the typically studied situation of shear between two layers, each with constant density that differ. Three cases with different strength of stratification in the deep region ($J_d = 0.10, 0.25$ and 1.0) and with uniform stratification ($J_s = 0.05$) in the shear zone are compared with a two-layer case. All four cases have the same overall bulk Richardson number $Ri_b = 0.10$.

The thickness of the shear zone measured with the vorticity thickness δ_ω increases with increasing time. The thickness δ_ω is the smallest in the case with the strongest stratification, $J_d = 1.0$. Unlike the two-layer case where the thickness asymptotes at late time, δ_ω has a secondary growth stage at late time with a moderate but noticeable growth rate. This secondary growth leads to a vigorous growth in bulk Richardson number Ri_b because the shear layer entrains heavier fluid at the bottom edge. At the end of the $J_d = 1.0$ simulation, $Ri_b \simeq 4$, an order of magnitude larger than the asymptotic value of $Ri_b = 0.32 \pm 0.06$ observed in the two-layer problem. Another measure of shear layer thickness is the momentum thickness δ_θ. The J_d cases have significantly smaller δ_θ with respect to the two-layer situation. Furthermore, the secondary growth of δ_θ in the J_d cases is much smaller than that of δ_ω. The shear layer stirs and mixes up the density field and, consequently, pycnoclines (regions with a strong change in density gradient) are formed at the edges of the layer. At the bottom edge, the pycnocline grows and then merges into the strong background stratification. The pycnocline at the top edge grows and then depletes in time. The deep stratification leads to an important qualitative difference in the profile of mean shear with respect to the two-layer case. The position of maximum shear shifts from its initial position at the centre of the shear layer downward towards the centre of the thermocline in contrast to the two-layer case where the maximum shear remains

at the centre. Lower momentum fluid that is transported to the pycnocline by stirring is unable to exchange its momentum with the higher momentum fluid because of the large stable stratification in the pycnocline and, as a result, the shear is enhanced. Even with the enhanced shear, the gradient Richardson number is much larger than the critical value of 0.25 in the pycnocline and, consequently, shear instabilities are prohibited. In the presence of a deep stratification the coherent structures break down shortly after their formation because the nonlinear pairing process, observed in the two-layer case, is inhibited.

The shear layer excites strong internal waves in the cases with $J_d = 0.25$ and 1.0. Waves are excited during both the early-time stage of KH instability and the late-time stage of three-dimensional turbulence. The early-time generation of internal waves is especially strong and their characteristics can be explained by linear theory: the horizontal wavenumber is given by the most unstable wavelength, i.e. the KH mode, the temporal frequency is that due to the bottom free stream moving over the approximately stationary KH rollers and the linear dispersion relationship for internal gravity waves predicts the observed angle of the phase lines (equivalently group velocity). In particular, the phase lines are observed to tilt at approximately $\theta = 32°–38°$ ($J_d = 0.25$) and 62°–68° ($J_d = 1.0$) to the vertical. The power spectrum of the early-time internal waves as function of temporal frequency and wavenumber is also found to be consistent with linear theory. $J_d > 0.18$ is the condition for the KH instability to excite propagating internal waves. Consequently, KH-generated internal waves are not observed when $J_d = 0.10$. However, the late-time turbulent stage does permit internal waves that are observed to span a wide range of wavenumbers, frequencies and phase angles in the generation region. The linear theory that was found to work well at early time does not explain the characteristics of the late-time waves. In agreement with previous laboratory and numerical studies of turbulence-generated waves, the phase lines in the deep propagation region cluster in a narrowband, approximately around 45°.

Internal waves, observed here to propagate in the bottom interior region, do not transport mass away or into the shear layer, consistent with linear wave theory, but are shown to constitute a significant pathway for energy transfer into the interior. The net mass gain, observed here, is the result of the molecular diffusive flux associated with the density gradient external to the shear layer. Nonetheless, internal waves extract momentum from the shear layer. Therefore, the evolution of the momentum thickness δ_θ shows asymmetry: the thickness grows less in the bottom portion where strong internal waves are generated. The extraction is most efficient in the case with $J_d = 0.25$. Measures of Reynolds stress in the deep region show that internal wave can carry up to 10 % of the initial momentum inside the shear layer. The significant drag causes the bottom part of the shear layer to decelerate. Along with momentum, waves also transport energy to the ambient. The internal wave energy flux is examined by comparing the terms in the vertically integrated turbulent kinetic energy equation. Case $J_d = 0.25$ shows the strongest energy flux and not $J_d = 1.0$ implying that there is a buoyancy frequency which is optimal with respect to wave energy flux. Integration of the kinetic energy budget over the simulated time shows that the internal waves are important to the energetics of the shear layer. The contribution of the wave energy flux can be up to 17 % of the production, 33 % of the dissipation and 75 % of the buoyancy flux. Therefore, internal waves provide an important route for transport of fluctuation energy from shear flow instabilities into the stratified interior with potentially important implications for energy pathways in the ocean and in the atmosphere.

<p style="text-align:center">REFERENCES</p>

ANDREWS, D. G. & McINTYRE, M. E. 1978 An exact theory of nonlinear waves on a Lagrangian-mean flow. *J. Fluid Mech.* **89**, 609–646.

BASAK, S. & SARKAR, S. 2006 Dynamics of a stratified shear layer with horizontal shear. *J. Fluid Mech.* **568**, 19–54.

BRUCKER, K. A. & SARKAR, S. 2007 Evolution of an initially turbulent stratified shear layer. *Phys. Fluids* **19**, 101105.

CAULFIELD, C. P. & PELTIER, W. R. 1994 Three dimensionalization of the stratified mixing layer. *Phys. Fluids* **6**, 3803–3805.

CAULFIELD, C. P. & PELTIER, W. R. 2000 The anatomy of the mixing transition in homogeneous and stratified free shear layers. *J. Fluid Mech.* **413**, 1–47.

D'ASARO, E. A., ERIKSEN, C. C., LEVINE, M. D., NIILER, P., A., PAULSON C. & MEURS, P. V. 1995 Upper-ocean inertial currents forced by a strong storm. Part I. Data and comparisons with linear theory. *J. Phys. Oceanogr.* **25**, 2909–2936.

DELONCLE, A., CHOMAZ, J. & BILLANT, P. 2007 Three-dimensional stability of a horizontally sheared flow in a stably stratified fluid. *J. Fluid Mech.* **570**, 297–305.

DIAMESSIS, P. J. & NOMURA, K. K. 2004 The structure and dynamics of overturns in stably stratified homogeneous turbulence. *J. Fluid Mech.* **499**, 197–229.

DOHAN, K. & SUTHERLAND, B. R. 2003 Internal waves generated from a turbulent mixed region. *Phys. Fluids* **15** (2), 488–498.

DRAZIN, P. G., ZATURSKA, M. B. & BANKS, W. H. H. 1979 On the normal modes of parallel flow of inviscid stratified fluid. Part 2. Unbounded flow with propagation at infinity. *J. Fluid Mech.* **95**, 681–705.

XUEQUAN, E. & HOPFINGER, E. J. 1986 On mixing across an interface in stably stratified fluid. *J. Fluid Mech.* **166**, 227–244.

EINAUDI, F., LALAS, D. P. & PERONA, G. E. 1978 The role of gravity waves in tropospheric processes. *Pure Appl. Geophys.* **117**, 627–663.

ELIASSEN, A. & PALM, E. 1960 On the transfer of energy in stationary mountain waves. *Geofys. Publ. (Geophys. Norv.)* **22**, 1–23.

ERIKSEN, C. 1982 Geostrophic equatorial deep jets. *J. Mar. Res.* **40**, 143–157.

FIRING, E. 1987 Deep zonal currents in the central equatorial Pacific. *J. Mar. Res.* **45**, 791–812.

FRITTS, D. 1982 Shear excitation of atmospheric gravity waves. *J. Atmos. Sci.* **39**, 1936–1952.

GERZ, T., SCHUMANN, U. & ELGHOBASHI, S. E. 1989 Direct numerical simulation of stratified homogeneous turbulent shear flows. *J. Fluid Mech.* **200**, 563–594.

HAZEL, P. 1972 Numerical studies of the stability of inviscid stratified shear flows. *J. Fluid Mech.* **51**, 39–61.

HOLT, S. E., KOSEFF, J. R. & FERZIGER, J. H. 1992 A numerical study of the evolution and structure of homogeneous stably stratified sheared turbulence. *J. Fluid Mech.* **237**, 499–539.

HOLTON, J. R., HAYNES, P. H., McINTYRE, M. E., DOUGLASS, A. R., ROOD, R. B. & PFISTER, L. 1995 Stratosphere–troposphere exchange. *Rev. Geophys.* **33**, 403–439.

JACOBITZ, F. G. & SARKAR, S. 1999a A direct numerical study of transport and anisotropy in a stably stratified turbulent flow with uniform horizontal shear. *Flow Turbul. Combust.* **63**, 343–360.

JACOBITZ, F. G. & SARKAR, S. 1999b On the shear number effect in stratified shear flow. *Theor. Comput. Fluid Dyn.* **13**, 171–188.

JACOBITZ, F. G., SARKAR, S. & VANATTA, C. W. 1997 Direct numerical simulations of the turbulence evolution in a uniformly sheared and stably stratified flow. *J. Fluid Mech.* **342**, 231–261.

JOHNSTON, T. & RUDNICK, D. 2009 Observations of the transition layer. *J. Phys. Oceanogr.* in press.

KALTENBACH, H.-J., GERZ, T. & SCHUMANN, U. 1994 Large-eddy simulation of homogeneous turbulence and diffusion in stably stratified shear flow. *J. Fluid Mech.* **280**, 1–40.

Koop, C. G. & Browand, F. K. 1979 Instability and turbulence in a stratified fluid with shear. *J. Fluid Mech.* **93**, 135–159.

Linden, P. F. 1975 The deepening of a mixed layer in a stratified fluid. *J. Fluid Mech.* **71**, 385–405.

Luyten, J. & Swallow, J. 1976 Equatorial undercurrents. *Deep Sea Res.* **23**, 499–524.

Monkewitz, P. A. & Huerre, P. 1982 Influence of the velocity ratio on the spatial instability of mixing layers. *Phys. Fluids* **25**, 1137–1143.

Moum, J. N., Hebert, D., Paulson, C. A. & Caldwell, D. R. 1992 Turbulence and internal waves at the equator. Part I. Statistics from towed thermistors and a microstructure profiler. *J. Phys. Oceanogr.* **22**, 1330–1345.

Oakey, N. S. 1985 Statistics of mixing parameters in the upper ocean during JASIN phase 2. *J. Phys. Oceanogr.* **15**, 1662–1675.

Osborn, T. R. 1980 Estimates of the local rate of vertical diffusion from dissipation measurements. *J. Phys. Oceanogr.* **10**, 80–89.

Piccirillo, P. & VanAtta, C. W. 1997 The evolution of a uniformly sheared thermally stratified turbulent flow. *J. Fluid Mech.* **334**, 61–86.

Rohr, J. J., Itsweire, E. C., Helland, K. N. & VanAtta, C. W. 1988 Growth and decay of turbulence in a stably stratified shear flow. *J. Fluid Mech.* **195**, 77–111.

Rosenlof, K. H. 1996 Summer hemisphere differences in temperature and transport in the lower stratosphere. *J. Geophys. Res.* **101**, 19129–19136.

Skyllingstad, E. D. & Denbo, D. W. 1994 The role of internal gravity waves in the equatorial current system. *J. Phys. Oceanogr.* **24**, 2093–2110.

Smyth, W. D. & Moum, J. N. 2000a Anisotropy of turbulence in stably stratified mixing layers. *Phys. Fluids* **12** (6), 1343–1362.

Smyth, W. D. & Moum, J. N. 2000b Length scales of turbulence in stably stratified mixing layers. *Phys. Fluids* **12** (6), 1327–1342.

Smyth, W. D. & Moum, J. N. 2002 Shear instability and gravity wave saturation in an asymmetrically stratified jet. *Dyn. Atmos. Oceans* **35**, 265–294.

Smyth, W. D., Moum, J. N. & Caldwell, D. R. 2001 The efficiency of mixing in turbulent patches: Inferences from direct simulations and microstrucure observations. *J. Phys. Oceanogr.* **31**, 1969–1992.

Staquet, C. 2000 Mixing in a stably stratified shear layer: two- and three-dimensional numerical experiments. *Fluid Dyn. Res.* **27**, 367–404.

Staquet, C. & Riley, J. J. 1989 A numerical study of a stably-stratified mixing layer. In *Turbulent Shear Flows 6*, pp. 381–397. Springer-Verlag.

Strang, E. J. & Fernando, H. J. S. 2001 Entrainment and mixing in stratified shear flows. *J. Fluid Mech.* **428**, 349–386.

Sun, C., Smyth, W. D. & Moum, J. N. 1998 Dynamic instability of stratified shear flow in the upper equatorial Pacific. *J. Geophys. Res.* **103**, 10323–10337.

Sutherland, B. R. 1996 Dynamic excitation of internal gravity waves in the equatorial oceans. *J. Phys. Oceanogr.* **26**, 2398–2419.

Sutherland, B. R. 2006 Rayleigh wave-internal wave coupling and internal wave generation above a model jet stream. *J. Atmos. Sci.* **63**, 1042–1055.

Sutherland, B. R. & Linden, P. F. 1998 Internal wave excitation from stratified flow over a thin barrier. *J. Fluid Mech.* **377**, 223–252.

Taylor, J. R. & Sarkar, S. 2007 Internal gravity waves generated by a turbulent bottom Ekman layer. *J. Fluid Mech.* **590**, 331–354.

Thorpe, S. A. 1973 Experiments on instability and turbulence in a stratified shear flow. *J. Fluid Mech.* **61**, 731–751.

Tse, K. L., Mahalov, A., Nicolaenko, B. & Fernando, H. J. S. 2003 Quasi-equilibrium dynamics of shear-stratified turbulence in a model tropospheric jet. *J. Fluid Mech.* **496**, 73–103.

Weller, R. A. & Plueddemann, A. J. 1996 Observations of the vertical structure of the oceanic boundary layer. *J. Geophys. Res.* **101**, 8789–8806.